FINAL REPORT

Active Tensor Magnetic Gradiometer System

SERDP Project MM-1514

NOVEMBER 2007

David V. Smith
Jeffrey D. Phillips
S. Raymond Hutton
U.S. Geological Survey

This document has been approved for public release.

Strategic Environmental Research and Development Program

For product and ordering information:

World Wide Web: http://www.usgs.gov/pubprod

Telephone: 1-888-ASK-USGS

For more information on the USGS—the Federal source for science about the Earth, its natural and living resources, natural hazards, and the environment:

World Wide Web: http://www.usgs.gov

Telephone: 1-888-ASK-USGS

Any use of trade, product, or firm names is for descriptive purposes only and does not imply endorsement by the U.S. Government.

Although this report is in the public domain, permission must be secured from the individual copyright owners to reproduce any copyrighted material contained within this report.

Suggested citation: Smith, D.V., Phillips, J.D., and Hutton, S.R, 2007, Active tensor magnetic gradiometer system final report for Project MM-1514: U.S. Geological Survey Administrative Report to the Strategic Environmental Research and Development Program

This report was prepared under contract to the Department of Defense Strategic Environmental Research and Development Program (SERDP). The publication of this report does not indicate endorsement by the Department of Defense, nor should the contents be construed as reflecting the official policy or position of the Department of Defense. Reference herein to any specific commercial product, process, or service by trade name, trademark, manufacturer, or otherwise, does not necessarily constitute or imply its endorsement, recommendation, or favoring by the Department of Defense.

Table of Contents

Introduction **1**

Modeling and Simulations **2**

Modify Forward Computer Models 2

Modify TMGS Simulator 3

Perform Simulations 5

Analyze Simulation Data 6

Theory and Algorithms **7**

Evaluate Multiple-Euler Algorithms and Helbig's Method 7

Develop Active-Mode Algorithms 20

Develop Discrimination Algorithms 24

Develop Induced/Remanence Algorithms 31

Engineering Assessment **38**

Primary Signal Generator 39

Alternative Sensor Technologies 43

Conclusions **45**

References Cited **46**

Table of Figures

Figure 1. Physical model of the ATMGS with dimensions shown. Coil separation distances are measured to the center of fluxgate sensing coils. 3

Figure 2. Nomenclature and coordinate convention used for the magnetometer heads and sensing axes. The inner and middle coils of the array sense different components, depending on the orientation of the magnetometer heads. The z-component is always sensed by the outer coils. 4

Figure 3. Example graphical user interface of a simulation run. Interactive controls are in the left panel. The targets and array trajectory are displayed in the right panel. 6

Figure 4. Data flow diagram for ATMGS data processing and analysis. 7

Figure 5. A, X (north), Y (east), and Z (vertical) magnetic field components produced by the three test dipoles of table 1. Circles indicate the dipole locations. B, Magnetic field components produced by the solution dipoles of table 2. 17

Figure 6. A, Five independent components of the magnetic gradient tensor for the three test dipoles of table 1. Circles indicate the dipole locations. B, Magnetic gradient tensor components produced by the solution dipoles of table 3. 18

Figure 7. Four 20-mm spheres buried 0.02 m deep along a single line were simulated here. The four spheres have the same magnetic permeability but different remanent magnetization (increasing from left to right). The top plot shows the z-component of head 1. Separation of the active signal (blue) from the static signal (purple) is achieved by simple high-pass and low-pass filtering, respectively. The inductive response for the four spheres is identical, but the static magnetic anomaly (bottom plot) from each differs according to their magnetic moments. 21

Figure 8. Example of simulated data along line over three 60-mm targets in the standard model. Shown are the received signal from head 1 z-component (red), the static signal (green), the active signal (blue) and the rectified (magenta) and demodulated signal (gray). 22

Figure 9. Close up of simulation data over a single 60-mm target in the standard model. Shown are the received signal from head 1 z-component (red), the static signal (purple), the active signal (blue) and the rectified (magenta) and demodulated signal (gray). 22

Figure 10. Map of head1 z-component only of static anomalies of six 60-mm targets in the standard model. 23

Figure 11. Demodulated (envelope) active component of six isolated 60-mm targets in the standard model. 24

Figure 12. Map of maxima/minima of active component selected for inversion to induced moments. The locations of different magnetic z-components (red, magenta, yellow, blue) are offset because of the physical separation of the fluxgate heads on the array. The lines are irregular because of terrain effects. 26

Figure 13. Recovered moments (Ms) versus actual induced moments (Mi). True moment values are slightly greater in magnitude than the moments recovered through inversion. 27

Figure 14. Effects of noise sources on recovered moments. Solid diamond is noise free; hollow blue square is with system noise; yellow triangle is with terrain effects; and red square is with both noise and terrain effects. 28

Figure 16. The ratio of length to width is diagnostic of whether a target is UXO-like or scrap-like. The 60-mm target has a ratio of 2. 30

Figure 17. Conceptual block diagram of the ATMGS..... 39

Figure 18. Conceptual block diagram of the active drive unit. Subsystems are labeled NI/PXI, K, I, C, and T. Kalman: See section, "Possible Sources of Improvement (NI/PXI)." 40

Active Tensor Magnetic Gradiometer System

Final Report for Project MM-1514

By David V. Smith, Jeffrey D. Phillips, and S. Raymond Hutton

Introduction

This report summarizes the work and results achieved under SERDP project MM-1514 entitled, "Active Tensor Magnetic Gradiometer System." The objective of the project was to prove the concept of an active tensor magnetic gradiometer system (ATMGS) using physics-based models and systems-based real-world simulations. Positive outcomes of this feasibility study were identified as: (1) a conceptual design at a functional system block diagram level, containing specific engineering design and operational parameters, and (2) a theoretical framework for analyzing and interpreting system data. Conceptual designs for an active magnetic gradient measurement system are based upon the existing tensor magnetic gradiometer system (TMGS) developed under project MM-1328 entitled, "Evaluation, Modification, and Testing of the Very Early Time Electromagnetic (VETEM) System, the High Frequency Sounder (HFS), and the Tensor Magnetic Gradiometer System (TMGS) for UXO Detection, Imaging, and Discrimination." The TMGS developed under MM-1328 was successfully tested at the Standardized Test Site at Yuma Proving Ground, Arizona, in 2005 over the Calibration Grid, a small test area seeded with inert ordnance and clutter. By modifying the prototype TMGS with an active magnetic source, unexploded ordnance (UXO) surveys can be performed in two modes simultaneously – passive and active. In the passive mode, tensor data will be acquired for all target and natural anomalies over an area. At the same time, tensor data will be acquired for an alternating magnetic field at a precisely driven frequency. In this active mode, data will be acquired only for targets in the near zone of the field generator. Active mode data can be used to identify the target's remanent magnetization. By simultaneously measuring static anomalies in a search area and active anomalies in closer proximity to the instrument, this approach has the potential to segregate UXO and clutter. By separating a target's remanent and induced magnetization, discrimination of UXO-like targets and scrap-like clutter can be improved (Billings, 2002).

Three distinct but related methods were used in this feasibility study. First, numerical computer models and simulations of various possible configurations of an ATMGS were developed and implemented. Simulation data were used as the basis for developing data processing and analysis routines. Second, theoretical approaches to analyzing ATMGS data were investigated. Third, engineering analyses were undertaken of sensors and interface electronics to determine those modifications necessary to implement a prototype ATMGS.

Modeling and Simulations

Modify Forward Computer Models

Because no instrumentation development or empirical experiments were proposed, a successful outcome depended on a realistic simulation of the TMGS with an active source. The ATMGS simulator was built upon the systems-based TMGS simulator already developed using ITT's Interactive Data Language (IDL)[1] because it has all the necessary features:

- Platform geometry: wheelbase, wheel diameter, array location and height, GPS location and height
- Array geometry: sensor geometry and baseline separation
- Sensor properties: axis offsets, inorthogonalities, noise
- System properties: sample rate, channel gains, noise
- Site size: variable dimensions
- Irregular (fractal) terrain model of relief
- Ground magnetization (natural anomalies as a vector field)
- Earth's main magnetic field model with diurnal variation
- Platform trajectory: variable line spacing with interactive speed and steering controls
- Targets: location, depth, magnetization vector
- Outputs: 12 vector components, 5 measured gradients, 6 true gradients, true total magnetic field at centroid of array, roll, pitch, fluxgate sensor location (x, y, z of each axis), array location (x, y, z of centroid), GPS location (x, y, z), and time base.

Relevant parameters of the simulation – 12 vector components, roll, pitch, fluxgate sensor location (x, y, z of each of 12 axes), array location (x, y, z of centroid), and time base – were used in the forward model that calculates the secondary field caused by a target at each of the 12 sensor locations. A dimensioned drawing of the physical model of the conceptual ATMGS is shown in figure 1. The dimensions of the sensor array are fixed, and the separation distance between individual coil pairs is shown. The primary field coil is helical, concentric with the fluxgate array, and has its mid-height in the plane of the individual sensing coils. The figure shows a 1.5 m diameter coil with 5-windings. The modeled coil has a finite height and thickness, both of which depend on the diameter of the wire specified. In this report, reference is made to individual triaxial magnetometers as Head 1, Head 2, Head 3, and Head 4. The layout of the heads and the sensing directions of the individual fluxgate coils are illustrated in figure 2. Note that different coil pairs are used in the longitudinal and lateral directions for the x- and y-vector baselines.

Limitations and assumptions include that inorthogonalities of the sensor axes in the array reference frame are taken as zero, and that the magnetic field values were not converted to the bin-number/error-voltage format of the real TMGS. We made the assumption that empirically measured calibration coefficients for the real system are sufficiently accurate to orthogonalize the axes and to convert from raw voltages to magnetic field magnitudes.

[1] Any use of trade, product, or firm names is for descriptive purposes only and does not imply endorsement by the U.S. Government.

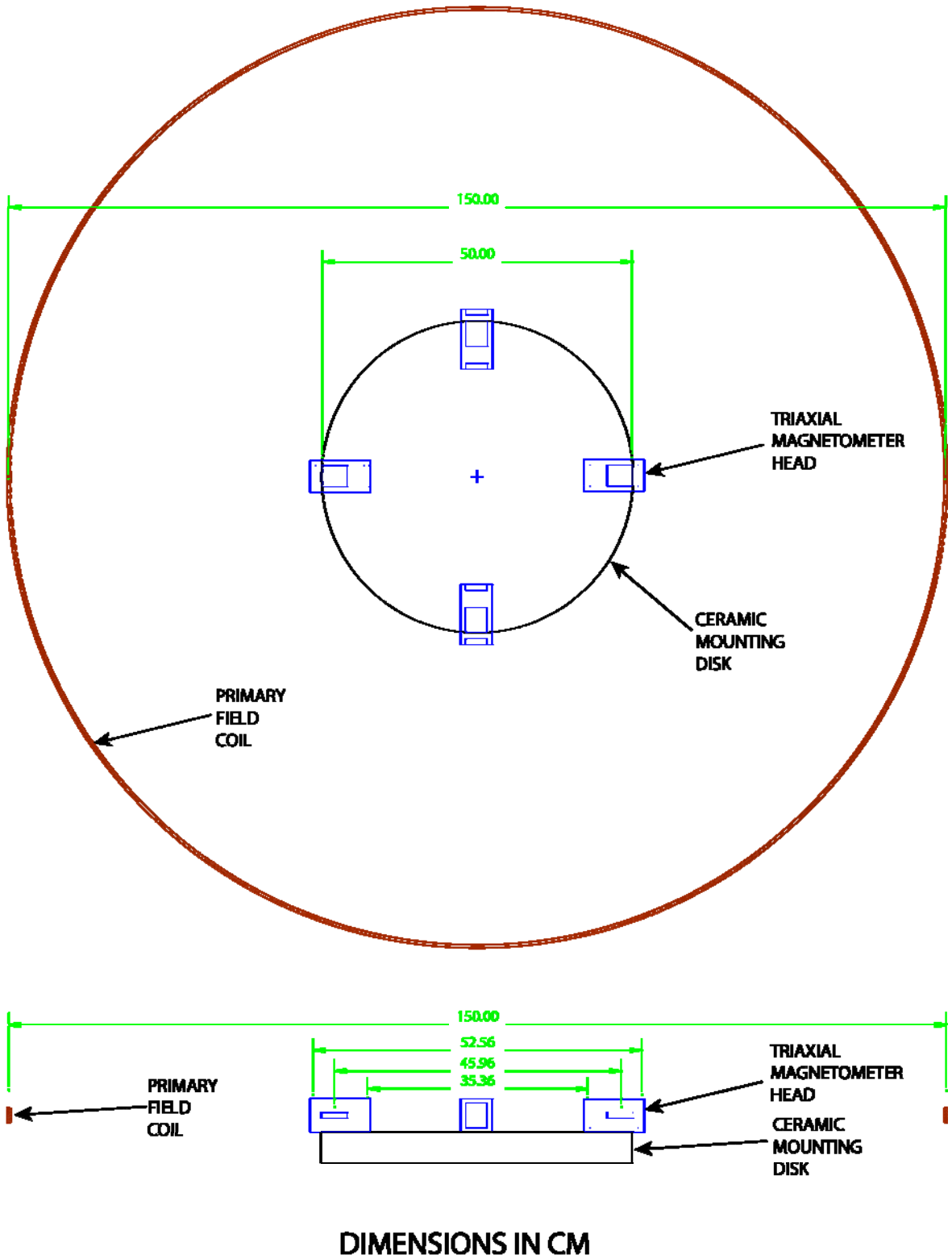

Figure 1. Physical model of the ATMGS with dimensions shown. Coil separation distances are measured to the center of fluxgate sensing coils.

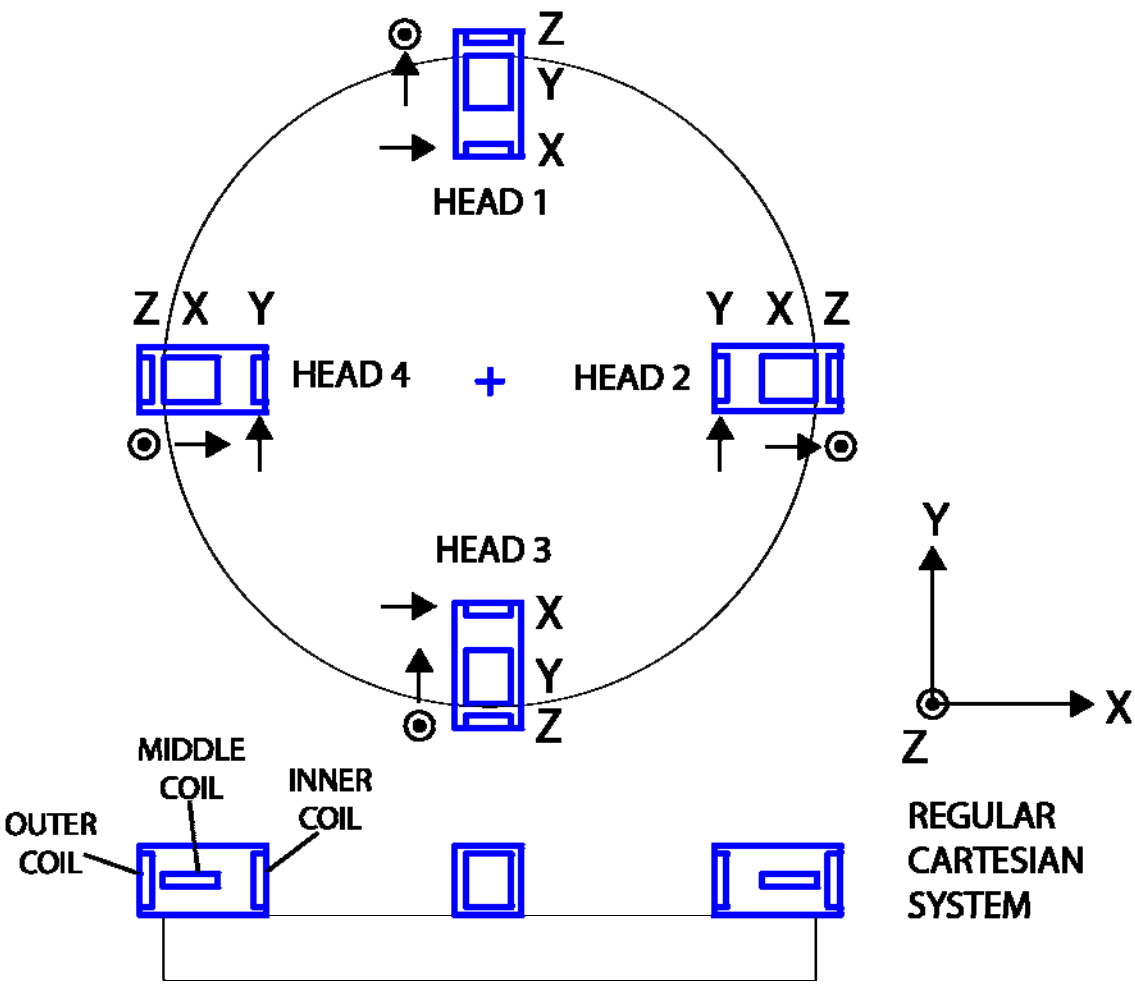

Figure 2. Nomenclature and coordinate convention used for the magnetometer heads and sensing axes. The inner and middle coils of the array sense different components, depending on the orientation of the magnetometer heads. The z-component is always sensed by the outer coils.

Modify TMGS Simulator

The original simulator was modified to include several software modules:

- Targets as spheroids: location (x, y, z), length (radius *a*), diameter (radius *c*), azimuth and dip of radius *a*, and magnetic permeability;
- Primary field generator (solenoid): coil diameter, height, wire gauge, number of turns, current, frequency;

- Primary field at target location: magnetic field components (Bx, By, Bz) calculated at target location using Biot-Savart law for the modeled solenoid; and
- Spheroidal induction: magnetization vectors (Mx, My, Mz) of a spheroid with radii *a* and *c* and azimuth and dip of radius *a* in an external magnetic field (Bx, By, Bz).

We made the assumption that the magnetic field at the spheroidal target's centroid is uniform over volume of target. This assumption is valid for small spheroids at distances approximately the diameter of the solenoid, but does not hold for closer targets or large spheroids. We assume the error in our simulations is negligible, although we offer no proof. This assumption was made to avoid the computational complexity and demands of an arbitrary spheroid in a non-uniform magnetic field. We also assume that, for typical UXO bodies, the total magnetization of a solid spheroid model is close to (to within 10 percent) that of a spheroidal shell model (Billings, 2002; Butler, 2001; Altshuler, 1996). Again, this assumption was made to avoid increased computational complexity.

Perform Simulations

The simulator can perform an unlimited number of scenarios with varied targets and terrains. This research concentrated on a very limited set of scenarios in order to develop and investigate data processing, analysis, and interpretation techniques. The following parameters constituted the standard scenario:

- Site dimensions: 10 by 10 meters,
- Trajectory: 0.25 m line spacing, traveling south-to-north at 2 m/s,
- Targets: six 60-mm spheroids at 0.2 m depth, equally spaced,
- Target orientations: three at 0 azimuth and 0, 30, 60 degrees dip; three at 90 azimuth and 0, 30, 60 degrees dip;
- Terrain: fractal surface with +/- 10 cm relief.

The following parameters modeled the ATMGS system:

- Planar cross array with paired magnetic component baselines of 35.36, 45.96, and 52.56 cm,
- Towed platform with dimensions of the cart used for tests at YPG,
- Sample rate: 900 Hz, and
- Sensor noise: 16 $pT/Hz^{1/2}$.

A graphical representation of a non-standard simulation run with 11 targets is shown in figure 3, where the targets are shown in red and the trajectory of the array is shown in green. The trajectory is irregular because of terrain effects.

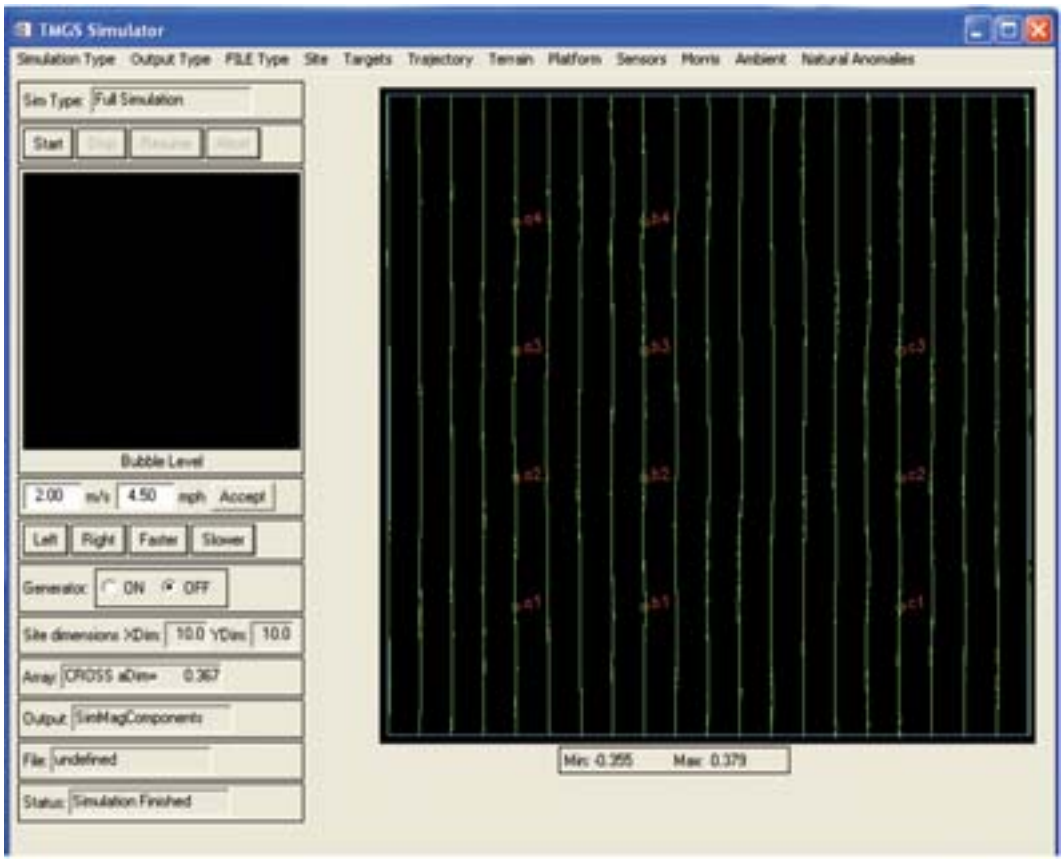

Figure 3. Example graphical user interface of a simulation run. Interactive controls are in the left panel. The targets and array trajectory are displayed in the right panel.

Analyze Simulation Data

Data files generated by the simulations were processed in Geosoft's Oasis montaj. This software has the capability of handling extremely large data sets efficiently, and contains tools for filtering, gridding and displaying time-series and spatial data. Oasis montaj was used to generate data sets containing position (x, y, z) and measured gradients (G_{ij}). USGS software was used to determine target location using Euler and Helbig analyses. IDL programs were used to calculate induced moments (Mx, My, Mz) at each location where the primary field was at a minimum or maximum. The maxima and minima were selected because dB/dt is zero. Therefore, magnetostatic equations can be applied. Knowing the location of the primary field generator, the array centroid, and the target, we made estimates of the target's spheroidal geometry based upon the spatial variation of the induced magnetic moments. The data flow diagram is given in figure 4.

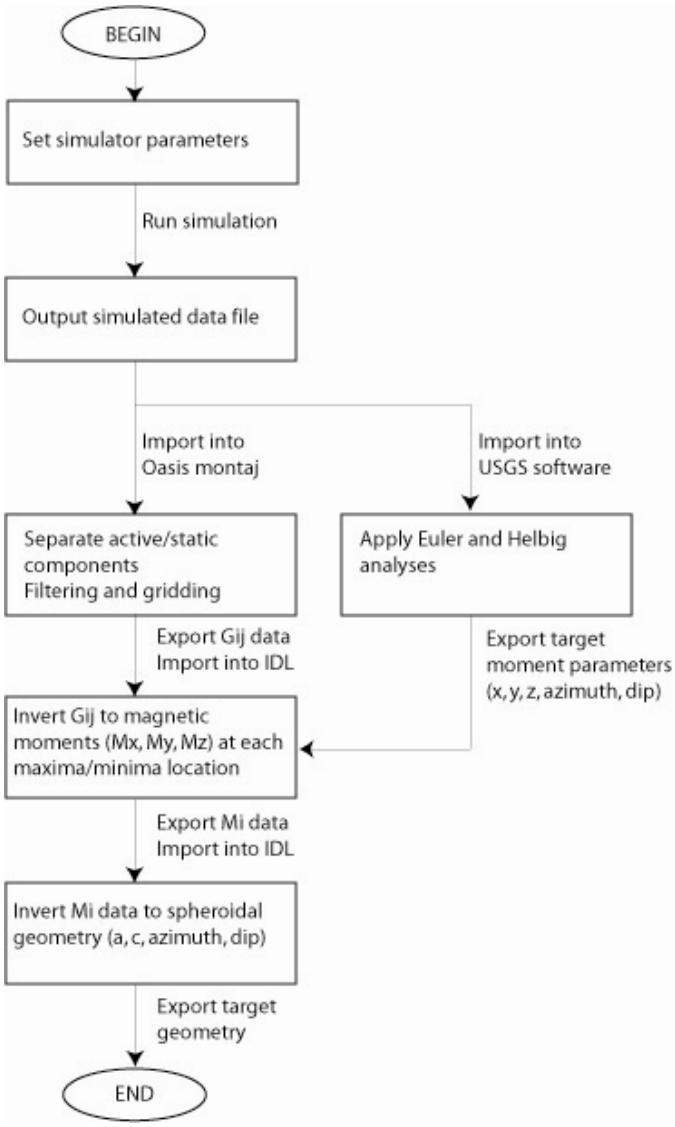

Figure 4. Data flow diagram for ATMGS data processing and analysis.

Theory and Algorithms

Evaluate Multiple-Euler Algorithms and Helbig's Method

Although Euler and Werner multiple-source algorithms have proven useful for locating UXO sources, they provide no additional physical property information about the sources. To determine the magnetic dipole moments and the magnetization (or elongation) directions of the sources, another approach is required. A first step we investigated involves implementing Helbig's method (Helbig, 1963), which

uses the first moments of magnetic vector components to estimate total magnetization directions. By using Helbig's method to estimate the total magnetization directions at the Euler source locations for each of the dual-mode data sets, it should be possible to separate the induced component of the magnetization from the remanent component for each source. Using the estimated source locations and the estimated magnetization directions, we can perform a linear inversion to estimate the magnetic susceptibility, the remanent magnetization, and the magnetic dipole moments of the sources.

Helbig's method has been successfully applied to geological problems (Schmidt and Clark, 1997, 1998), and has been implemented by the USGS for total-field magnetic data (Phillips, 2005, Phillips and others, 2007). It works best on dipole sources that have adequate horizontal separation for the first moments to be reliably estimated. Application of Helbig's method to the passive mode data of the tensor survey should be straightforward, providing estimates of total magnetization directions and magnetic dipole moments for the sources. Application to the active mode data should allow separation of the total magnetization into induced and remanent components, but will involve the complication that the inducing field direction varies over the source distribution.

The total magnetization of a magnetic source is the vector sum of the remanent magnetization and the induced magnetization. The Helbig method, as implemented by Phillips (2005), is useful for estimating the horizontal positions and the total magnetization directions of compact magnetic sources from measured or calculated magnetic vector field components.

In the following exposition (Phillips and others, 2007) we extend the Helbig method in several ways. First, we show how the method can be modified so that magnetic gradient tensor measurements can be used instead of magnetic vector component measurements. Next, we show how, given the horizontal positions of the sources, a simplified version of the Euler equation, applied in windows, can be used to estimate the depths to the compact sources under the assumption that they are magnetic dipoles. Finally, we show how a linear least-squares fit to the data can be used to determine the dipole moments of the sources.

This extended Helbig approach can be used to locate and characterize compact magnetic sources such as ore bodies, UXO, and abandoned wells. It may also prove useful for removing some cultural noise, such as strong, localized anomalies produced by steel buildings, from aeromagnetic data.

The Helbig Method

In the Helbig method (Helbig, 1963; Schmidt and Clark, 1997, 1998; Phillips, 2005), the first moments of vector magnetic field components are used to estimate the direction of the total magnetization. The magnetic field components can be derived from total-field magnetic data using Fourier filters.

Using the Helbig integrals, total magnetization directions can be estimated in small data windows centered on each grid node of the magnetic vector field component grids. If the central grid node lies over a compact source that can be represented by a magnetic dipole, then the calculated magnetization direction will accurately predict the total magnetization direction of the dipole, and the direction will remain relatively constant as the window size is increased in small steps. On the other hand, if the central grid node does not lie over a source, the calculated total magnetization direction will change with increasing window size.

We can locate the grid nodes where the estimated magnetization direction is relatively insensitive to window size by setting a threshold for the maximum allowable angular change in the direction between successive window sizes, then counting the number of successive window sizes that produce solutions with angular changes below this threshold. Grid nodes with large counts identify source locations; those with small counts identify source-free areas. With this approach, the Helbig method can be used to estimate the horizontal positions of the compact sources as well as their total magnetization directions.

By averaging the magnetization directions for the solutions that fall below the threshold, we get an estimate of the total magnetization direction at each grid node. This estimate will be accurate only at grid nodes that lie over sources, that is, those with large counts. However, between sources the estimated magnetization directions will be continuous. This means that the Helbig method can also be used to produce a continuous estimate of the magnetization direction over a magnetic survey area, which can then be sampled at source locations determined using a second method, such as Euler deconvolution (Reid and others, 1990).

The Helbig method is based on the observation (Helbig, 1963) that the vector components (m_x, m_y, m_z) of the total magnetization of a compact source can be estimated from the first moments of the vector components (B_x, B_y, B_z) of the anomalous magnetic field produced by the source. Here we use the convention of geomagnetism that the x-axis points north, the y-axis points east, and the z-axis points down. The first moments are evaluated as infinite integrals over the horizontal plane.

$$
\begin{aligned}
m_x &= -\frac{1}{2\pi}\int_{-\infty}^{\infty}\int_{-\infty}^{\infty} x\,B_z(x,y)\,dx\,dy \\
m_y &= -\frac{1}{2\pi}\int_{-\infty}^{\infty}\int_{-\infty}^{\infty} y\,B_z(x,y)\,dx\,dy \qquad (1) \\
m_z &= -\frac{1}{2\pi}\int_{-\infty}^{\infty}\int_{-\infty}^{\infty} x\,B_x(x,y)\,dx\,dy = -\frac{1}{2\pi}\int_{-\infty}^{\infty}\int_{-\infty}^{\infty} y\,B_y(x,y)\,dx\,dy
\end{aligned}
$$

The other two first moments are zero, as are the integrals (mean values) of B_x, B_y, and B_z over the plane. We refer to these five integrals as Helbig's vanishing integrals.

Phillips (2005) has shown that, in order to estimate total magnetization directions using the integrals of equation set (1) within a finite data window, it is necessary to satisfy Helbig's vanishing integrals within the finite window by removing a planar surface from the magnetic vector component within the window. This assures that the mean values of the components are zero within the window, and that the vanishing moments are approximately zero.

Extending the Helbig Method to Magnetic Gradient Measurements

This requirement to estimate and remove planar surfaces from each magnetic vector component in the finite data window, while computationally straightforward, does represent a burden when many overlapping data windows of different sizes are used in the analysis. In an attempt to relax this

requirement, we can consider using first- or second-order derivatives of the magnetic vector components for Helbig analysis. First-order derivatives of the components are measured directly by tensor magnetic gradiometer systems, such as those currently being evaluated for application to the detection of UXO and for commercial mineral exploration.

To develop Helbig equations for derivatives of the magnetic vector components, we can use integration-by-parts on the integrals of (1). For example, the m_x component can be expressed as either

$$\begin{aligned} m_x &= -\frac{1}{2\pi}\int_{-\infty}^{\infty}\int_{-\infty}^{\infty} x\,B_z(x,y)\,dx\,dy \\ &= -\frac{1}{2\pi}\int_{-\infty}^{\infty}\left[\int_{-\infty}^{\infty} B_z(x,y)\,x\,dx\right]dy \\ &= -\frac{1}{2\pi}\int_{-\infty}^{\infty}\left[B_z(x,y)\frac{x^2}{2}\bigg|_{-\infty}^{\infty} - \int_{-\infty}^{\infty}\frac{x^2}{2}\frac{\partial B_z}{\partial x}dx\right]dy \end{aligned} \tag{2}$$

or

$$\begin{aligned} m_x &= -\frac{1}{2\pi}\int_{-\infty}^{\infty}\int_{-\infty}^{\infty} x\,B_z(x,y)\,dx\,dy \\ &= -\frac{1}{2\pi}\int_{-\infty}^{\infty}\left[\int_{-\infty}^{\infty} B_z(x,y)\,x\,dy\right]dx \\ &= -\frac{1}{2\pi}\int_{-\infty}^{\infty}\left[B_z(x,y)xy\bigg|_{-\infty}^{\infty} - \int_{-\infty}^{\infty} xy\frac{\partial B_z}{\partial y}dy\right]dx \end{aligned} \tag{3}$$

If the vertical component B_z of the magnetic field decays more rapidly than the square of the distance, which is the case for all compact magnetic sources, then the first terms in the square brackets are zero. It follows that (1) can be rewritten in terms of second moments of first derivatives of the magnetic vector components as,

$$\begin{aligned} m_x &= \frac{1}{4\pi}\int_{-\infty}^{\infty}\int_{-\infty}^{\infty} x^2\frac{\partial B_z}{\partial x}dx\,dy = \frac{1}{2\pi}\int_{-\infty}^{\infty}\int_{-\infty}^{\infty} xy\frac{\partial B_z}{\partial y}dx\,dy \\ m_y &= \frac{1}{4\pi}\int_{-\infty}^{\infty}\int_{-\infty}^{\infty} y^2\frac{\partial B_z}{\partial y}dx\,dy = \frac{1}{2\pi}\int_{-\infty}^{\infty}\int_{-\infty}^{\infty} xy\frac{\partial B_z}{\partial x}dx\,dy \\ m_z &= \frac{1}{4\pi}\int_{-\infty}^{\infty}\int_{-\infty}^{\infty} x^2\frac{\partial B_x}{\partial x}dx\,dy = \frac{1}{4\pi}\int_{-\infty}^{\infty}\int_{-\infty}^{\infty} y^2\frac{\partial B_y}{\partial y}dx\,dy \\ &= \frac{1}{2\pi}\int_{-\infty}^{\infty}\int_{-\infty}^{\infty} xy\frac{\partial B_x}{\partial y}dx\,dy = \frac{1}{2\pi}\int_{-\infty}^{\infty}\int_{-\infty}^{\infty} xy\frac{\partial B_y}{\partial x}dx\,dy \end{aligned} \tag{4}$$

The partial derivatives represent components that can be directly measured with a tensor magnetic gradient system. In terms of standard symmetric tensor notation,

$$\frac{\partial B_x}{\partial x} = B_{xx}, \frac{\partial B_y}{\partial y} = B_{yy}, \frac{\partial B_x}{\partial y} = \frac{\partial B_y}{\partial x} = B_{xy} = B_{yx}, \frac{\partial B_z}{\partial x} = B_{zx} = B_{xz}, \frac{\partial B_z}{\partial y} = B_{zy} = B_{yz} \qquad (5)$$

In addition to being useful for tensor magnetic gradient measurements, equation set (4) has the advantage over equation set (1) that, in order to evaluate the integrals within finite data windows and still satisfy Helbig's vanishing integrals, it is necessary to remove only the mean value from each tensor component within the window.

Because equation set (4) provides at least two estimates for each magnetization component, it allows for some measure of the reliability of each component. For example, the two estimates of m_x can be combined into a mean value and an uncertainty in the mean as

$$\hat{m}_x = \frac{1}{2}(\hat{m}_{x1} + \hat{m}_{x2}) \pm \frac{1}{2}(\hat{m}_{x1} - \hat{m}_{x2}) \qquad (6)$$

This is an improvement over equation set (1), which only provides a measure of the uncertainty in the m_z component.

When the magnetization components are estimated in a finite window, it turns out that the two estimates of m_x are not strictly equivalent. Instead, there are two sets of components, one from the integrals starting with $1/2\pi$ and one from the integrals starting with $1/4\pi$. The two sets produce magnetization vectors with identical directions but slightly different magnitudes. Details are given in the section, "Supplemental Summary of Helbig's Non-Vanishing Integrals" on page 17.

Starting from (4), the integration-by-parts can be repeated to generate a third set of equations for the magnetization components, this time in terms of third moments of second derivatives of the vector components.

$$
\begin{aligned}
m_x &= -\frac{1}{12\pi}\int_{-\infty}^{\infty}\int_{-\infty}^{\infty} x^3 \frac{\partial^2 B_z}{\partial x^2}\,dx\,dy = -\frac{1}{4\pi}\int_{-\infty}^{\infty}\int_{-\infty}^{\infty} x^2 y \frac{\partial^2 B_z}{\partial x \partial y}\,dx\,dy \\
&= -\frac{1}{4\pi}\int_{-\infty}^{\infty}\int_{-\infty}^{\infty} xy^2 \frac{\partial^2 B_z}{\partial y^2}\,dx\,dy \\
m_y &= -\frac{1}{12\pi}\int_{-\infty}^{\infty}\int_{-\infty}^{\infty} y^3 \frac{\partial^2 B_z}{\partial y^2}\,dx\,dy = -\frac{1}{4\pi}\int_{-\infty}^{\infty}\int_{-\infty}^{\infty} xy^2 \frac{\partial^2 B_z}{\partial x \partial y}\,dx\,dy \\
&= -\frac{1}{4\pi}\int_{-\infty}^{\infty}\int_{-\infty}^{\infty} x^2 y \frac{\partial^2 B_z}{\partial x^2}\,dx\,dy \\
m_z &= -\frac{1}{12\pi}\int_{-\infty}^{\infty}\int_{-\infty}^{\infty} x^3 \frac{\partial^2 B_x}{\partial x^2}\,dx\,dy = -\frac{1}{12\pi}\int_{-\infty}^{\infty}\int_{-\infty}^{\infty} y^3 \frac{\partial^2 B_y}{\partial y^2}\,dx\,dy \\
&= -\frac{1}{4\pi}\int_{-\infty}^{\infty}\int_{-\infty}^{\infty} x^2 y \frac{\partial^2 B_x}{\partial x \partial y}\,dx\,dy = -\frac{1}{4\pi}\int_{-\infty}^{\infty}\int_{-\infty}^{\infty} xy^2 \frac{\partial^2 B_y}{\partial x \partial y}\,dx\,dy \\
&= -\frac{1}{4\pi}\int_{-\infty}^{\infty}\int_{-\infty}^{\infty} x^2 y \frac{\partial^2 B_y}{\partial x^2}\,dx\,dy = -\frac{1}{4\pi}\int_{-\infty}^{\infty}\int_{-\infty}^{\infty} xy^2 \frac{\partial^2 B_x}{\partial y^2}\,dx\,dy
\end{aligned}
\tag{7}
$$

The second derivative terms cannot be measured directly, but they can be calculated from the vector components or from the tensor magnetic gradient components. The integrals can be evaluated in finite data windows without removing any surfaces or constants from the second derivative terms.

As with the first derivative case, components estimated using a finite window fall into multiple sets. One set of components is estimated from the integrals starting with $1/2\pi$, one from the integrals starting with $1/4\pi$, and one from the integrals starting with $1/12\pi$. The three sets produce magnetization vectors with identical directions but slightly different magnitudes. Details are given in the section, "Supplemental Summary of Helbig's Non-Vanishing Integrals" on page 17.

The Euler Equation

In the previous section, we showed how the Helbig method can be extended to work with tensor magnetic gradient components instead of vector magnetic field components. In either case, the Helbig method can provide estimates of the horizontal source locations and total magnetization directions of the compact sources. To fully characterize the sources, their depths and magnetic moments must be estimated.

If the horizontal locations (x_0, y_0) of a dipole source are known, the Euler equation (Reid and others, 1990) can be used to estimate the depth z_0 of the dipole and a constant β representing interference from adjacent sources.

$$z_0 \frac{\partial T}{\partial z} + \beta = (x - x_0)\frac{\partial T}{\partial x} + (y - y_0)\frac{\partial T}{\partial y} + nT \qquad (6)$$

Here n=3 for a dipole source and T is the total field anomaly. This equation can be solved in the least-squares sense using data in small windows (3x3, 5x5, 7x7, …) centered on the known horizontal location of each dipole source. The solution that produces the shallowest z_0 is probably the best.

An alternative approach would involve solutions using the vector components (B_x, B_y, B_z) computed for the Helbig method and the magnetic potential (V) computed as the negative of the first vertical integral of B_z:

$$z_0 B_z + \beta = (x - x_0)B_x + (y - y_0)B_y + nV \qquad (7)$$

In this case n=2 for a dipole source.

For the case of magnetic gradient tensor measurements or calculated derivatives of vector components, there are three Euler equations (Zhang and others, 2000):

$$\begin{aligned} z_0 B_{zz} + \beta_z &= (x - x_0)B_{zx} + (y - y_0)B_{zy} + nB_z \\ z_0 B_{xz} + \beta_x &= (x - x_0)B_{xx} + (y - y_0)B_{xy} + nB_x \\ z_0 B_{yz} + \beta_y &= (x - x_0)B_{yx} + (y - y_0)B_{yy} + nB_y \end{aligned} \qquad (8)$$

or, equivalently

$$\begin{aligned} z_0 \frac{\partial B_z}{\partial z} + \beta_z &= (x - x_0)\frac{\partial B_z}{\partial x} + (y - y_0)\frac{\partial B_z}{\partial y} + nB_z \\ z_0 \frac{\partial B_x}{\partial z} + \beta_x &= (x - x_0)\frac{\partial B_x}{\partial x} + (y - y_0)\frac{\partial B_x}{\partial y} + nB_x \\ z_0 \frac{\partial B_y}{\partial z} + \beta_y &= (x - x_0)\frac{\partial B_y}{\partial x} + (y - y_0)\frac{\partial B_y}{\partial y} + nB_y \end{aligned} \qquad (9)$$

These equations are analogous to (6), so n=3 for a dipole source.

In a second approach, mentioned earlier, the Helbig method can be used to provide a continuous estimate of the total magnetization direction throughout the survey area, then this estimate can be sampled at source locations determined using a second magnetic source location method. Candidates for this second method include full Euler deconvolution as described by Reid and others (1990), various modifications of Euler deconvolution using Hilbert transforms and multiple sources, and non-Euler approaches using special functions such as the total gradient or the local wavenumber (Phillips and others, 2007).

Dipole Moments

Once the total magnetization directions, the horizontal locations, and the depths of the sources have been established, the dipole moments of the sources can be estimated by linear least-squares inversion. For example, if $U_i(x,y)$ represents the calculated field component or tensor component of the i-th source with unit dipole moment and $O(x,y)$ is the observed field component or tensor component produced by all N sources, then the unknown dipole moments m_i will satisfy

$$\sum_{i=1}^{N} U_i(x,y)m_i = O(x,y) + c \qquad (10)$$

in the least-squares sense, where c is an unknown constant.

Examples

Example 1 – Using (Noise-Free) Magnetic Field Components

To test the method, we used the three dipole sources described in table 1. The calculated field component grids are shown in figure 5*a*. The grids have a sample interval of 0.05 m.

The Helbig method was applied to the field components using the following approach. The Helbig integrals of (1) were evaluated in small windows centered on each grid node and having odd dimensions increasing from 3x3 to 25x25. For field components, a planar surface was removed from the component data within each window before the integration. The algorithm looked for successive solutions with increasing window size for which the total magnetization direction varied by less than a specified threshold of one degree in this case. For the grid nodes corresponding to the three dipole sources, at least 11 successive solutions with variations of less than one degree were found. For all other grid nodes, the number of successive solutions with variations of less than one degree was far fewer, between zero and six. To estimate the total magnetization direction, the successive solutions with variations of less than the threshold were averaged. The results, for averages with more than six solutions, are shown in table 2.

The simplified Euler equation (7) was used to estimate the depths of the sources. The equation was evaluated in windows of odd sizes from 3x3 to 13x13 centered on the sources. The shallowest solution

for each source was selected. A magnetic potential calculated from the true sources was used. Results are shown in the "depth" column of table 2.

The dipole moments were estimated from the three field components using a least-squares inversion, and are shown in the "moment" column of table 2. The calculated components from the estimated sources in table 2 are shown in figure 5*b*.

Example 2 – using (noise-free) tensor magnetic gradient components

The three dipole sources of table 1 were used to calculate the tensor magnetic gradient components shown in Figure 6*a*. The Helbig integrals in (4) were evaluated in small windows centered on each grid node and having odd dimensions increasing from 3x3 to 25x25. For tensor gradient components, a mean value was removed from the gradient component data within each window before the integration. Again the algorithm looked for successive solutions with increasing window size for which the total magnetization direction varied by less than a specified threshold of one degree. The only solutions found were at the grid nodes corresponding to the three dipole sources. At these nodes between 8 and 10 successive solutions with variations of less than one degree were found. To estimate the total magnetization direction, the successive solutions with variations of less than the threshold were averaged. The results are shown in table 3.

The Euler equations in (8) were used to estimate the depths of the sources. The equations were evaluated in windows of odd sizes from 3x3 to 13x13 centered on the sources. The shallowest solution for each source was selected. Magnetic field components calculated from the true sources were used. Results are shown in the "depth" column of table 3.

The dipole moments were estimated from the five independent gradient tensor components using a least-squares inversion, and are shown in the "moment" column of table 3. The calculated gradient tensor components from the estimated sources in table 3 are shown in figure 6*b*.

Table 1. Dipole source parameters used to test the method.

source	easting	northing	depth	inclination	declination	moment
1	1.0	1.0	0.20	0	30	0.020
2	2.0	1.0	0.25	60	-30	0.025
3	1.5	2.0	0.30	90	0	0.030

Table 2. Results of inversion using the magnetic field components.
[The eastings, northings, inclinations, and declinations are from Helbig analysis. The depths are from Euler analysis. The dipole moments are from least-squares inversion]

source	easting	northing	depth	inclination	declination	moment
1	1.0	1.0	0.191	0.427	30.063	0.0182
2	2.0	1.0	0.247	60.149	-29.881	0.0294
3	1.5	2.0	0.300	89.454	4.108	0.0400

Table 3. Results of inversion using the tensor magnetic gradient components.
[The eastings, northings, inclinations, and declinations are from Helbig analysis. The depths are from Euler analysis. The dipole moments are from least-squares inversion]

source	easting	northing	depth	inclination	declination	moment
1	1.0	1.0	0.200	0.071	30.055	0.0201
2	2.0	1.0	0.250	60.154	-30.056	0.0300
3	1.5	2.0	0.300	89.738	-1.541	0.0400

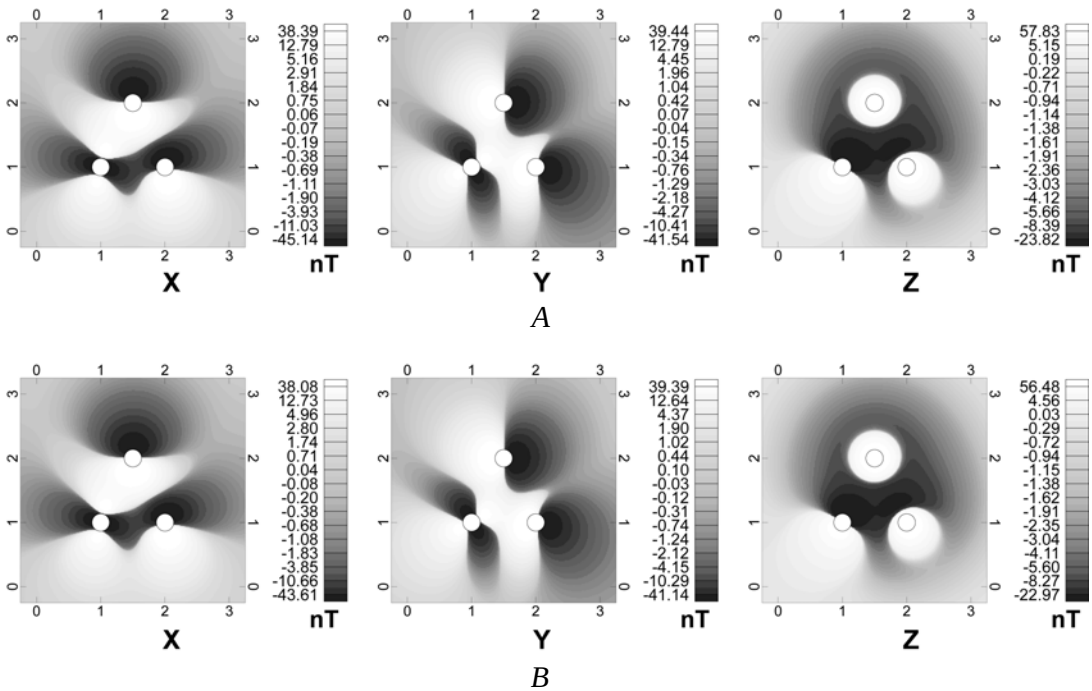

Figure 5. *A*, X (north), Y (east), and Z (vertical) magnetic field components produced by the three test dipoles of table 1. Circles indicate the dipole locations. *B*, Magnetic field components produced by the solution dipoles of table 2.

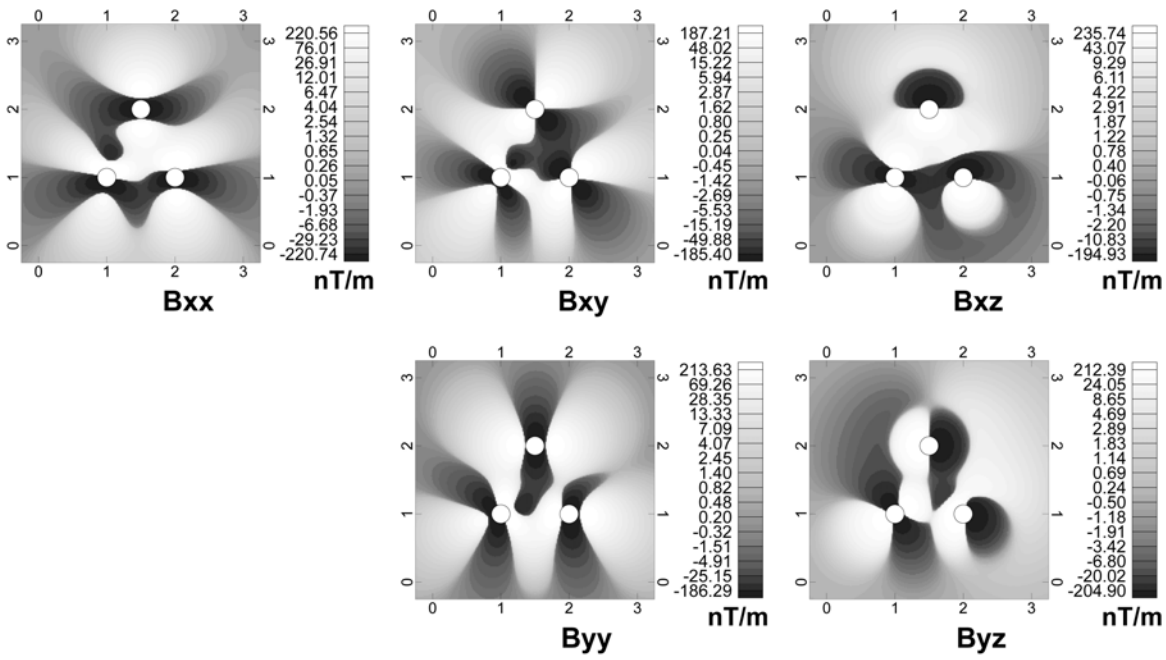

A

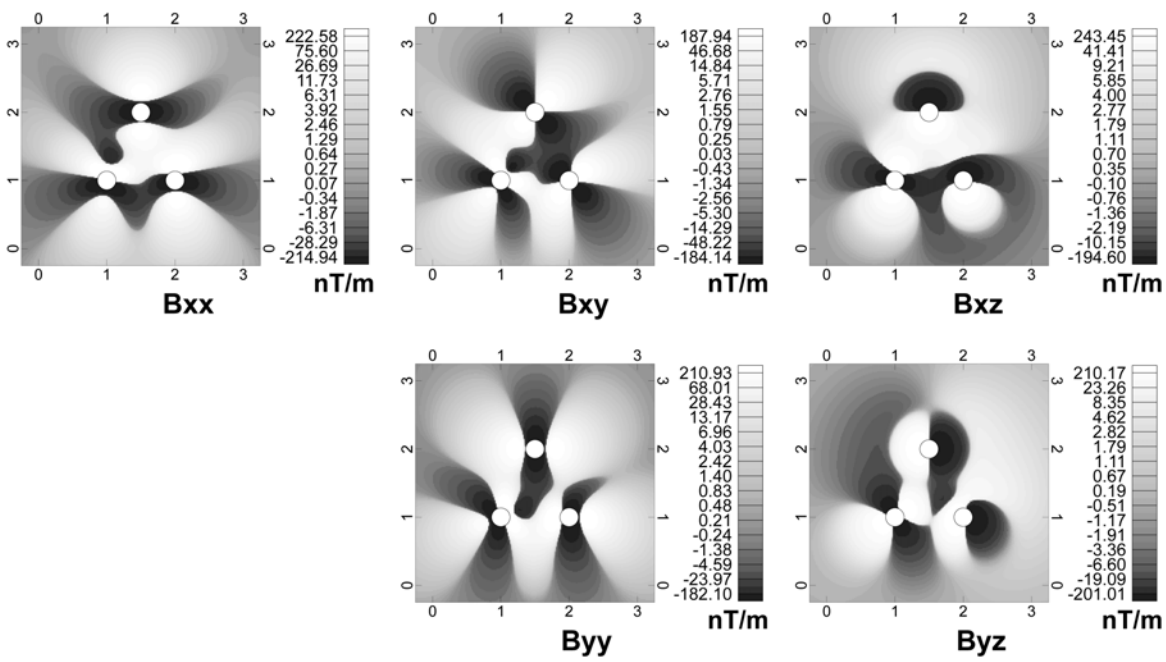

B

Figure 6. *A*, Five independent components of the magnetic gradient tensor for the three test dipoles of table 1. Circles indicate the dipole locations. *B*, Magnetic gradient tensor components produced by the solution dipoles of table 3.

Supplemental Summary of Helbig's Non-Vanishing Integrals

Let the bivariate moments of function *f(x,y)* be expressed as

$$b_{ij} f = \int_{-\infty}^{\infty}\int_{-\infty}^{\infty} x^i y^j f(x,y)\,dx\,dy \qquad \text{(A1)}$$

and let derivatives of the magnetic field components be expressed as

$$\frac{\partial B_z}{\partial x} = B_{zx}, \quad \frac{\partial^2 B_z}{\partial x^2} = B_{zxx} \qquad \text{(A2)}$$

Then the components of the total magnetization for a compact source can be expressed in terms of the bivariate moments of the field components, the first horizontal derivatives of the field components, and the second horizontal derivatives of the field components as

$$\begin{aligned}
m_x &= -\frac{1}{2\pi} b_{10} B_z \\
&= \frac{1}{4\pi} b_{20} B_{zx} = \frac{1}{2\pi} b_{11} B_{zy} \\
&= -\frac{1}{12\pi} b_{30} B_{zxx} = -\frac{1}{4\pi} b_{21} B_{zxy} = -\frac{1}{4\pi} b_{12} B_{zyy} \\
m_y &= -\frac{1}{2\pi} b_{01} B_z \\
&= \frac{1}{4\pi} b_{02} B_{zy} = \frac{1}{2\pi} b_{11} B_{zx} \qquad \text{(A3)} \\
&= -\frac{1}{12\pi} b_{03} B_{zyy} = -\frac{1}{4\pi} b_{12} B_{zxy} = -\frac{1}{4\pi} b_{21} B_{zxx} \\
m_z &= -\frac{1}{2\pi} b_{10} B_x = -\frac{1}{2\pi} b_{01} B_y \\
&= \frac{1}{4\pi} b_{20} B_{xx} = \frac{1}{4\pi} b_{02} B_{yy} = \frac{1}{2\pi} b_{11} B_{xy} = \frac{1}{2\pi} b_{11} B_{yx} \\
&= -\frac{1}{12\pi} b_{30} B_{xxx} = -\frac{1}{12\pi} b_{03} B_{yyy} = -\frac{1}{4\pi} b_{21} B_{xxy} = -\frac{1}{4\pi} b_{12} B_{yxy} = -\frac{1}{4\pi} b_{21} B_{yxx} = -\frac{1}{4\pi} b_{12} B_{xyy}
\end{aligned}$$

To estimate m_x, m_y, m_z using small data windows, it is best to use square windows. To approximately satisfy Helbig's vanishing integrals, planar surfaces should be removed from the field components B_x, B_y, B_z within the window; mean values should be removed from the first horizontal derivatives of the field components B_{xx}, B_{xy}, B_{yx}, B_{yy}, B_{zx}, B_{zy} within the window; and nothing needs to be removed from the second horizontal derivatives within the window. Even with these corrections, numerical experiments show that the various estimates for each magnetization component are not equivalent when finite windows are used.

There is one set of total magnetization components that can be estimated from the field components:

$$m_x = -\frac{1}{2\pi} b_{10} B_z \qquad m_y = -\frac{1}{2\pi} b_{01} B_z \qquad m_z = -\frac{1}{2\pi} b_{10} B_x = -\frac{1}{2\pi} b_{01} B_y \qquad \text{(A4)}$$

There are two sets that can be estimated from the first horizontal derivatives of the field components:

$$\begin{aligned} m_{x1} &= \frac{1}{4\pi} b_{20} B_{zx} & m_{y1} &= \frac{1}{4\pi} b_{02} B_{zy} & m_{z1} &= \frac{1}{4\pi} b_{20} B_{xx} = \frac{1}{4\pi} b_{02} B_{yy} \\ m_{x2} &= \frac{1}{2\pi} b_{11} B_{zy} & m_{y2} &= \frac{1}{2\pi} b_{11} B_{zx} & m_{z2} &= \frac{1}{2\pi} b_{11} B_{xy} = \frac{1}{2\pi} b_{11} B_{yx} \end{aligned} \qquad \text{(A5)}$$

In a given window, these two magnetization vectors will have equivalent directions but different magnitudes. There are three sets that can be estimated from the second horizontal derivatives of the components:

$$\begin{aligned} m_{x1} &= -\frac{1}{12\pi} b_{30} B_{zxx} & m_{y1} &= -\frac{1}{12\pi} b_{03} B_{zyy} & m_{z1} &= -\frac{1}{12\pi} b_{30} B_{xxx} = -\frac{1}{12\pi} b_{03} B_{yyy} \\ m_{x2} &= -\frac{1}{4\pi} b_{21} B_{zxy} & m_{y2} &= -\frac{1}{4\pi} b_{12} B_{zxy} & m_{z2} &= -\frac{1}{4\pi} b_{21} B_{xxy} = -\frac{1}{4\pi} b_{12} B_{yxy} \\ m_{x3} &= -\frac{1}{4\pi} b_{12} B_{zyy} & m_{y3} &= -\frac{1}{4\pi} b_{21} B_{zxx} & m_{z3} &= -\frac{1}{4\pi} b_{21} B_{yxx} = -\frac{1}{4\pi} b_{12} B_{xyy} \end{aligned} \qquad \text{(A6)}$$

These three magnetization vectors will have equivalent directions but different magnitudes in any given window.

It follows that in order to estimate total magnetization direction from the field components, you must have B_z and either B_x or B_y. In order to estimate total magnetization direction from the first horizontal derivatives of the field components, you must have both B_{zx} and B_{zy}, and one of B_{xx}, B_{yy}, B_{xy}, or B_{yx}. In order to estimate total magnetization direction from the second horizontal derivatives of the field components, you must have both B_{zxx} and B_{zyy}, and one of B_{xxx}, B_{yyy}, B_{yxx}, or B_{xyy}, or you must have B_{zxy} (B_{zyx}) and either B_{xxy} (B_{xyx}) or B_{yxy} (B_{yyx}).

Develop Active-Mode Algorithms

The primary field generator is synchronized with the data acquisition system so that secondary fields are measured at primary field maxima and minima, when dB/dt is zero. A target's location and static magnetic moment (remanent moment) are first estimated using Euler and Helbig methods. Knowing the primary coil current and radial vector to a target, one can calculate the induction field at the target's location. The induction field causes the target's total moment to rotate, which is simultaneously measured by the TMGS array. The demodulated active signal can locate ferrous targets with small or negligible remanent magnetization, as shown in figure 7.

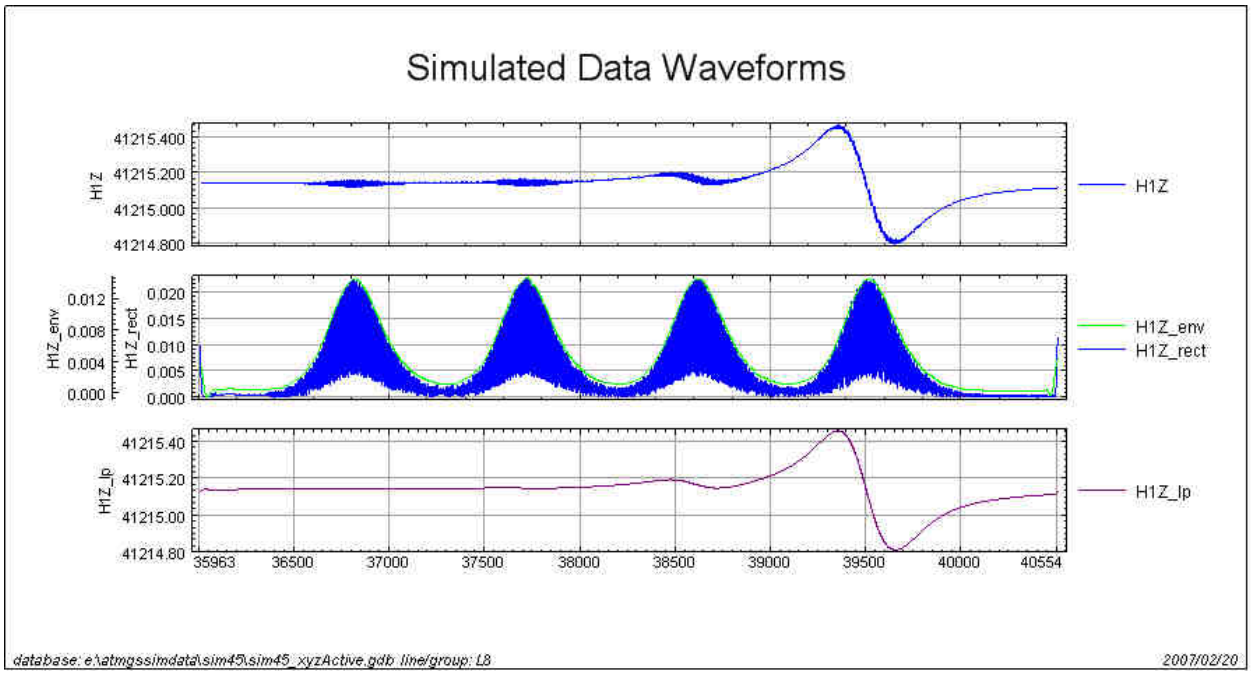

Figure 7. Four 20-mm spheres buried 0.02 m deep along a single line were simulated here. The four spheres have the same magnetic permeability but different remanent magnetization (increasing from left to right). The top plot shows the *z*-component of head 1. Separation of the active signal (blue) from the static signal (purple) is achieved by simple high-pass and low-pass filtering, respectively. The inductive response for the four spheres is identical, but the static magnetic anomaly (bottom plot) from each differs according to their magnetic moments.

Figure 8 shows plots of the ATMGS received signal (red) and the static (green) and active (blue) waveforms for the head 1 *z*-component along a line over three targets in the standard model. The bottom panel plots the rectified active signal (magenta) and its demodulation or envelope (gray). The primary field oscillation can be seen in the close-up in figure 9. The low-pass signal is the static magnetic field over the targets. A vector sum of the three orthogonal magnetic components of a single magnetometer head produces a total field map, as shown in figure 10. The total field data can be processed and gridded using standard potential field algorithms, such as those contained in the magmap.omn and ux-detect.omn utility menus in Oasis montaj. By contrast, the envelope provides a means of mapping isolated ferrous targets with sharp definition, as illustrated in figure 11.

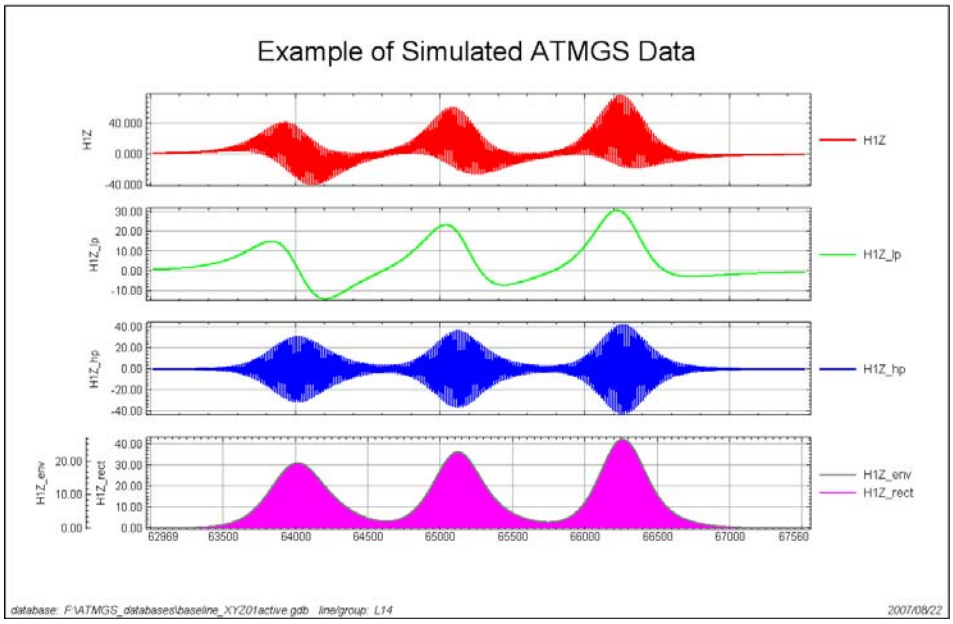

Figure 8. Example of simulated data along line over three 60-mm targets in the standard model. Shown are the received signal from head 1 *z*-component (red), the static signal (green), the active signal (blue) and the rectified (magenta) and demodulated signal (gray).

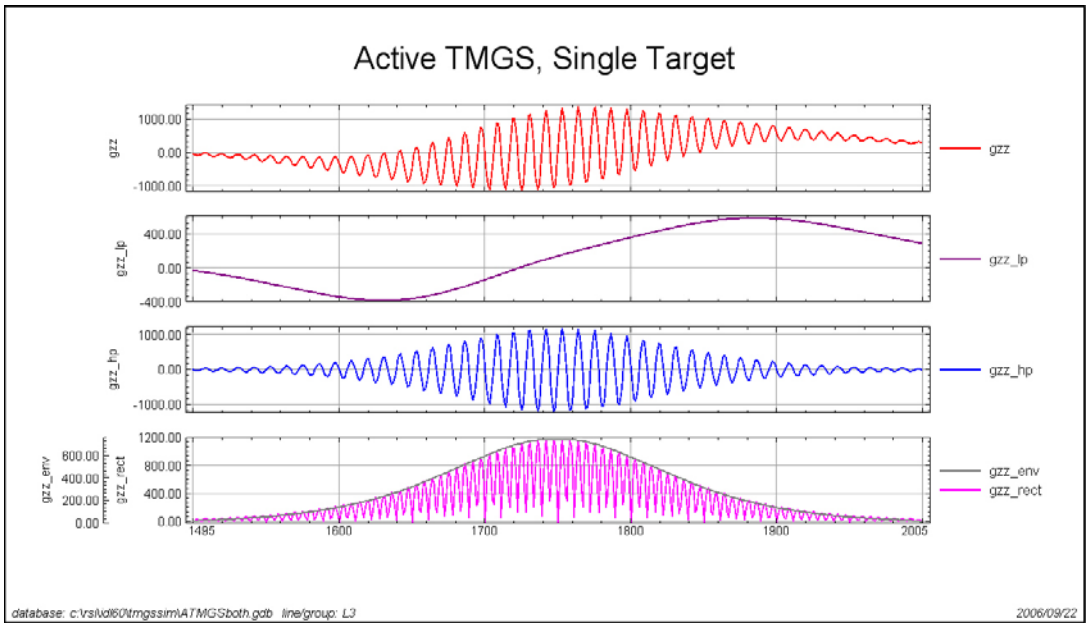

Figure 9. Close up of simulation data over a single 60-mm target in the standard model. Shown are the received signal from head 1 *z*-component (red), the static signal (purple), the active signal (blue) and the rectified (magenta) and demodulated signal (gray).

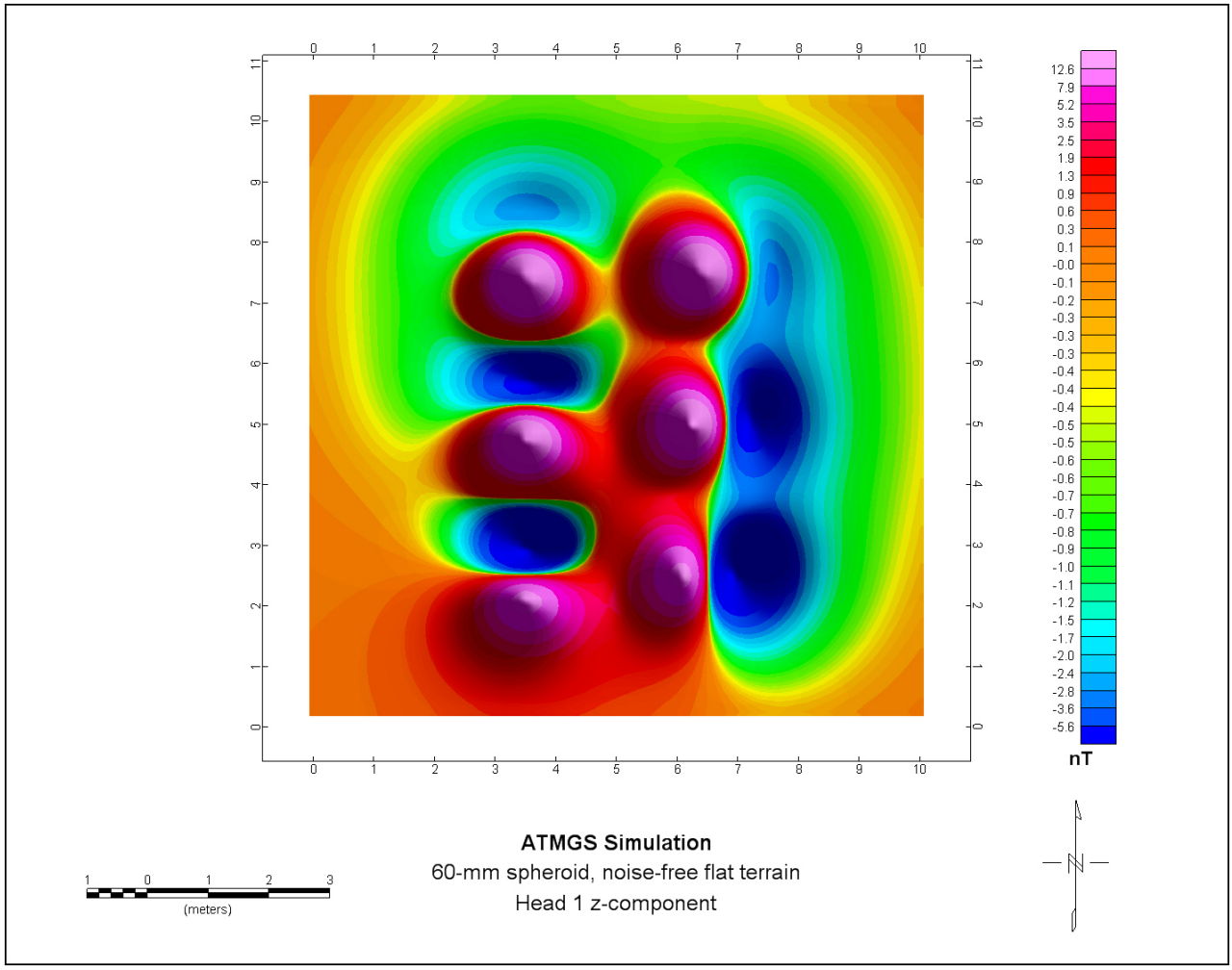

Figure 10. Map of head1 *z*-component only of static anomalies of six 60-mm targets in the standard model.

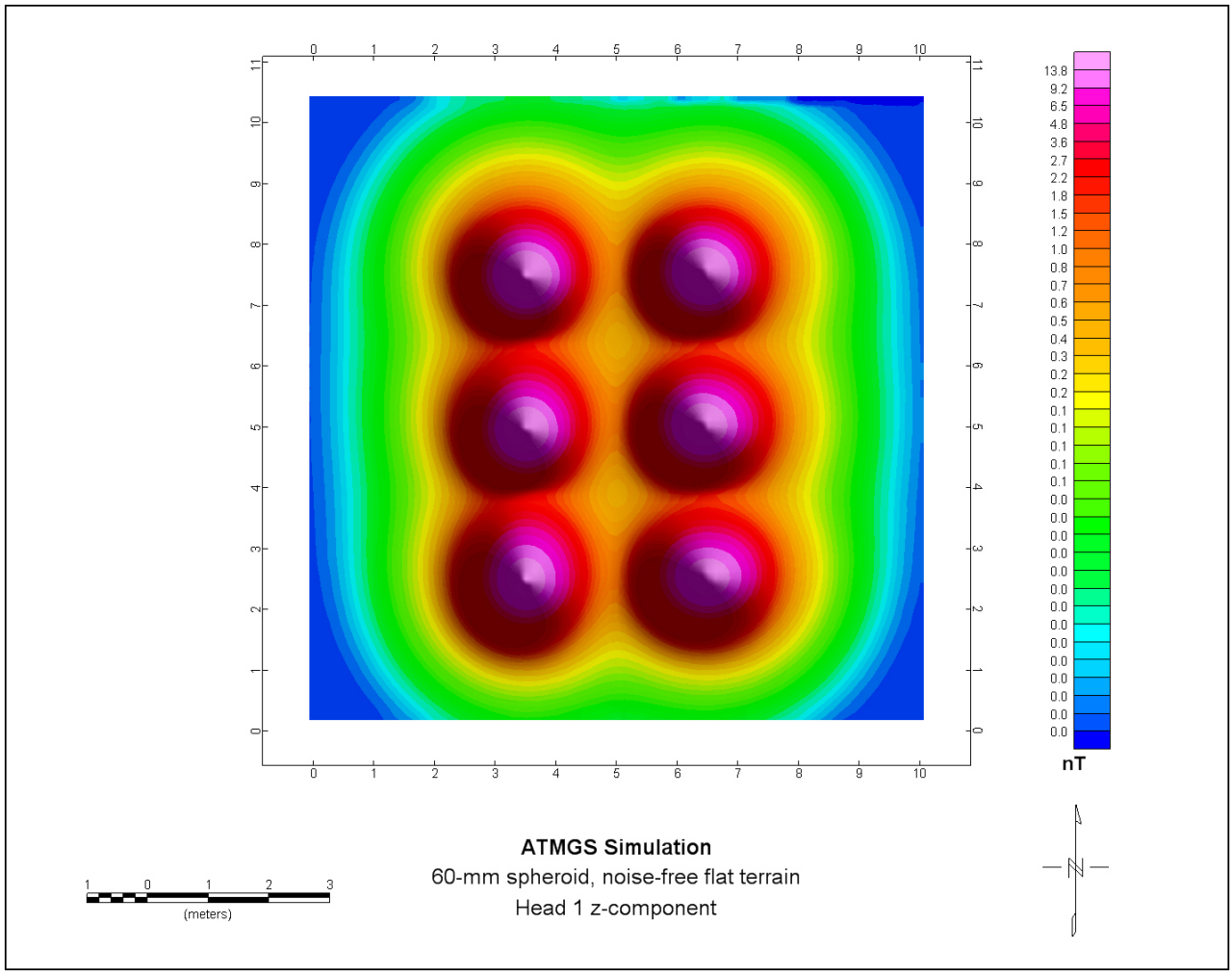

Figure 11. Demodulated (envelope) active component of six isolated 60-mm targets in the standard model.

This research project investigated what information can be gleaned from the active signals and the active signal gradients G_{ij} calculated by differencing opposite pairs of magnetometer axes and dividing by their baseline separation. A following section describes analysis of active tensor data in an attempt to separate the remanent and induced magnetization of a ferrous body. This section describes research into determining the spheroidal geometry of a target from active magnetic gradient data, and thereby discriminate UXO-like targets from scrap-like targets.

Develop Discrimination Algorithms

The problem of discrimination using magnetics has focused mainly on estimating the remanent magnetic moment of a target by looking at the magnitude and direction of its dipole moment and plotting those values against what would be expected of a purely induced moment in a degaussed target in the Earth's ambient field (Billings, 2002). The assumed degaussing occurs as shock demagnetization

when the ordnance item strikes the ground. This method has been shown to improve discrimination of intact UXO and clutter by 50 percent.

We take a different approach that uses all the information provided by the ATMGS. Because six discrete magnetic gradients G_{ij} are measured simultaneously at 900 readings per second, it is possible to pick the G_{ij} that occur at minima and maxima of the primary drive field over a target. At these instants, the primary field is at maximum magnitude and dB/dt is zero. Therefore, purely magnetostatic equations apply to the magnetic induction of a spheroidal body. As noted before, intact UXO can be adequately approximated by a spheroid, and a hollow spheroid can be adequately approximated by a solid spheroid. A simple thresholding technique on the magnetic *z*-components can isolate the G_{ij} used to invert for the instantaneous magnetic moment. The result of this selection over a single target is shown in figure 12, in which different colors correspond to the *z*-component of different magnetometer heads.

At each of the measurement locations, the six G_{ij} are inverted to solve for the magnetic moment (Mx, My, Mz) at the target location. A comparison of the inversion solutions (Ms) to the true induced moments (Mi) is plotted in figure 13. This is for the ideal case of no noise and horizontal, flat terrain. The agreement, though quite close, is not exact. The addition of system noise and terrain effects causes further divergence between the ideal and the more realistic cases, as illustrated in figure 14. The worst case combines system noise and terrain effects.

Having determined the induced moment at each measurement location, we find it possible to invert to a spheroidal model using the following procedure:

- Knowing the location and attitude of the sensor array and primary coil at each measurement point, calculate the *r*-vectors to the target's location.
- Calculate the magnetic field components of the primary coil at the target's location for each *r*-vector.
- Knowing the *r*-vectors, the induced moments, and the primary coil magnetic field components, invert to a magnetically permeable spheroid at the target's location.

The result of this procedure on the worst case simulation is given in figure 15 for spheroids with a diameter c of 60 mm but differing lengths a. Plate-like bodies are simulated by oblate spheroids with $a << c$, whereas rod-like bodies are simulated by prolate spheroids with $a >> c$. UXO-like bodies have an a:c ratio of between 2 and 4. Simulation scenarios 1-5 for maximum primary field strength (maxima in the active signal) are increasingly prolate, as compared to scenarios 6-9 which are increasingly oblate. This pattern repeats for scenarios 10-18, which are solutions for minimum primary field strength (minima in the active signal). Because of symmetry, the positive and negative solutions are very nearly identical. The 60-mm target spheroid is represented by scenario 1 and scenario 10. Figure 16 shows the results plotted against the ratio a:c, where the 60-mm target's ratio is 2.

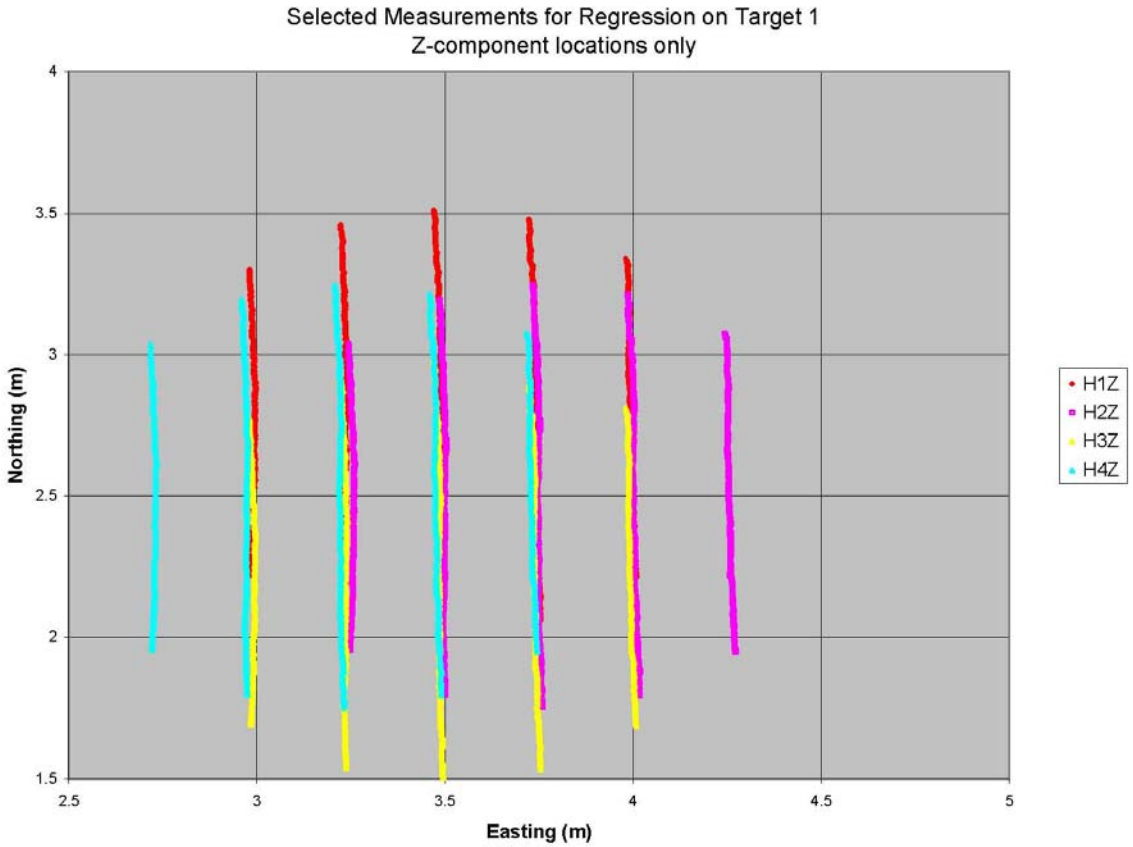

Figure 12. Map of maxima/minima of active component selected for inversion to induced moments. The locations of different magnetic *z*-components (red, magenta, yellow, blue) are offset because of the physical separation of the fluxgate heads on the array. The lines are irregular because of terrain effects.

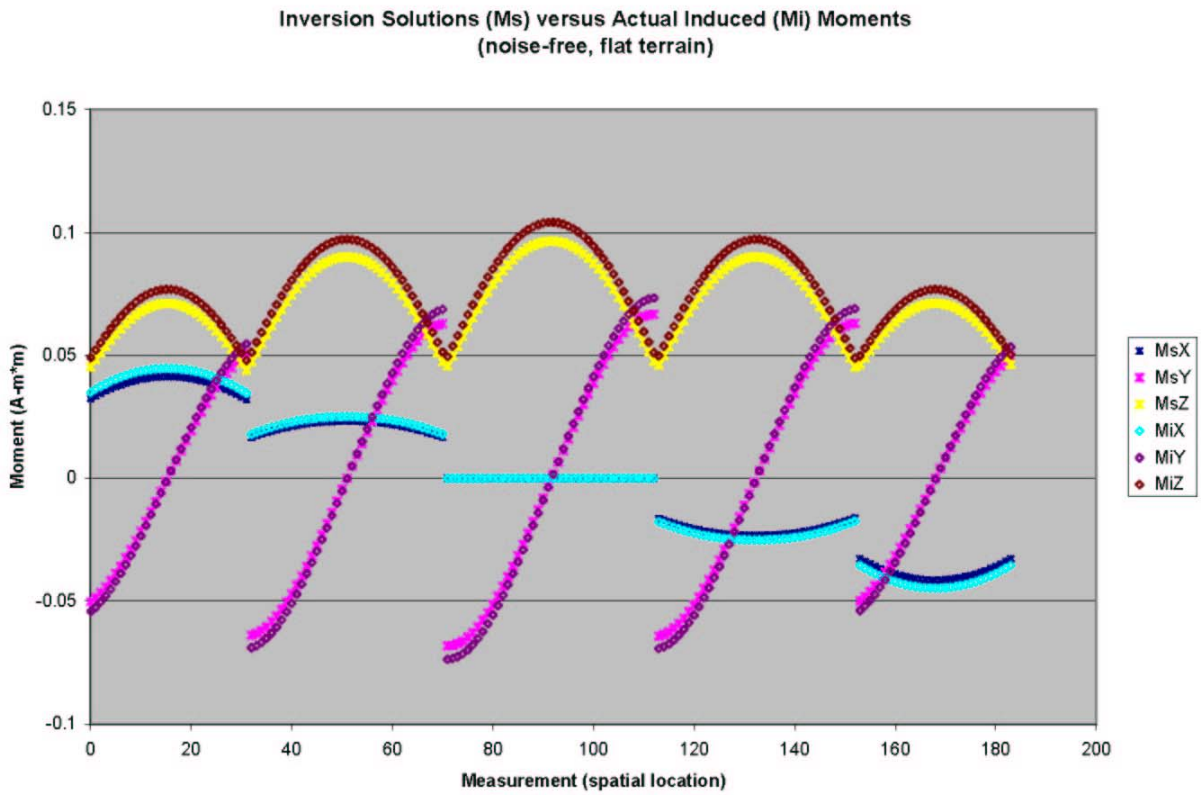

Figure 13. Recovered moments (*Ms*) versus actual induced moments (*Mi*). True moment values are slightly greater in magnitude than the moments recovered through inversion.

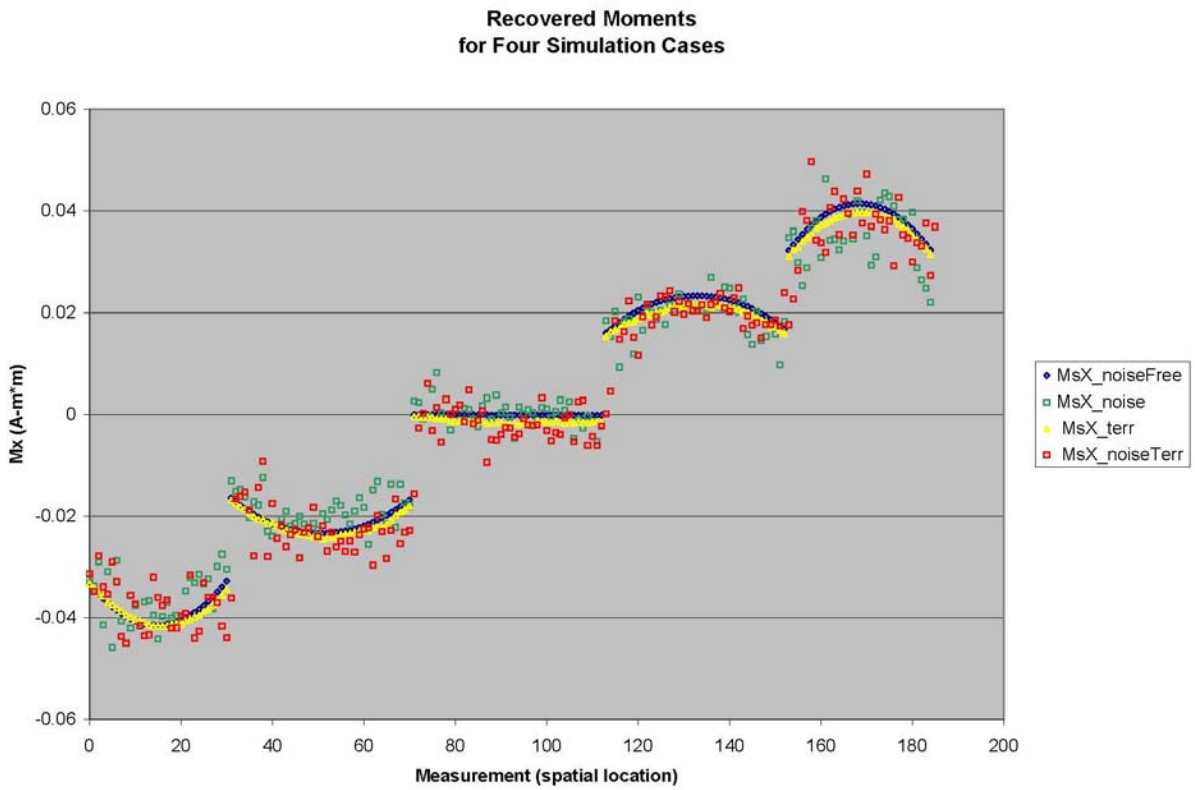

Figure 14. Effects of noise sources on recovered moments. Solid diamond is noise free; hollow blue square is with system noise; yellow triangle is with terrain effects; and red square is with both noise and terrain effects.

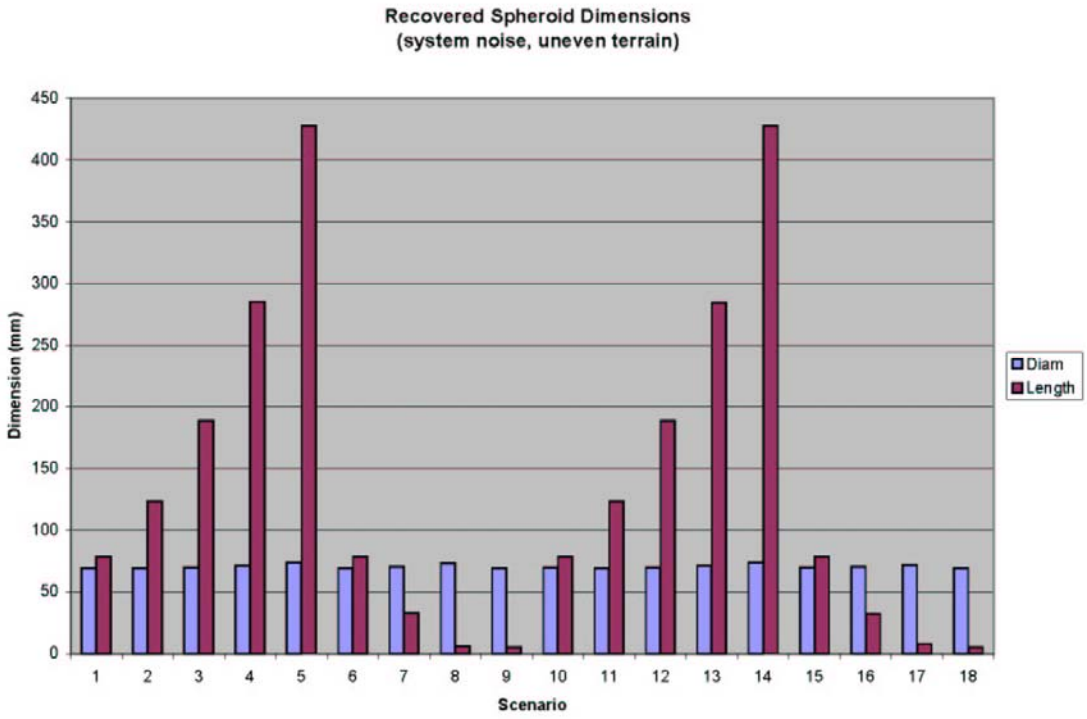

Figure 15. Recovered spheroid dimensions for modeled spheroids. Scenario 1 and scenario 10 represent the 60-mm spheroid. Scenarios 1-5 are increasingly prolate, whereas scenarios 6-9 are increasingly oblate. Scenarios 1-9 are solutions based on primary field maxima, and scenarios 10-18 are from primary field minima.

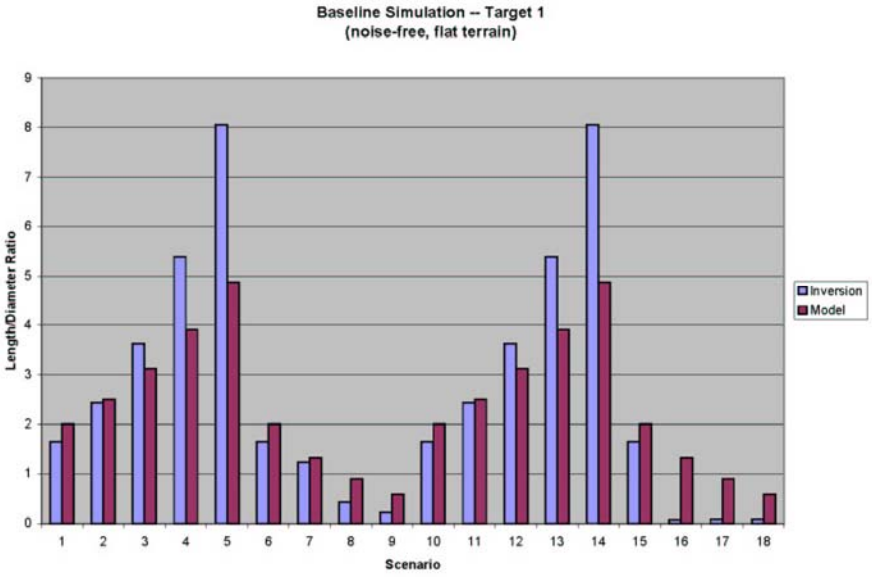

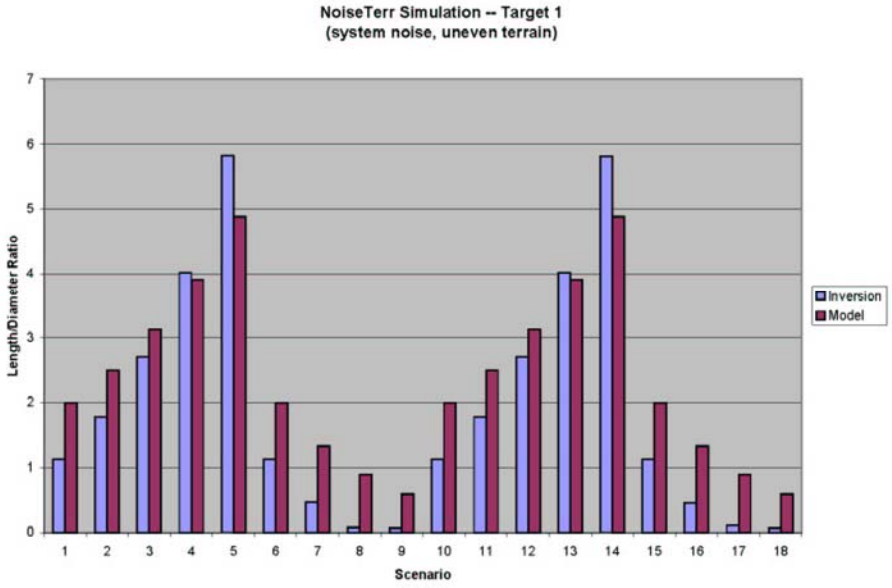

Figure 16. The ratio of length to width is diagnostic of whether a target is UXO-like or scrap-like. The 60-mm target has a ratio of 2.

Develop Induced/Remanence Algorithms

Two Helbig-Euler simulations were run with rectangular source bodies to test the ability of the active system to recover the moments, susceptibilities, and Koenigsberger ratios of non-dipole sources. The Koenigsberger ratio Q is defined as the ratio of the remanent magnetization to the induced magnetization. One simulation involved rod-like sources, the other involved plate-like sources.

The rod simulation involved three rectangular rods 5 units long by 1 unit by 1 unit oriented along the east, north, and vertical axes, three rectangular rods 3 units long by 1 unit by 1 unit also oriented along the east, north, and vertical axes, and three 1-unit cubes. One unit equals 0.25 m. The centers of the sources were 4 units below the sensors. The rods had remanent magnetizations oriented along their long axes, and the three cubes had remanent magnetizations in the three orthogonal directions. The remanent magnetization intensities were set so that the equivalent dipole moments of the sources were roughly the same. The model is described in table 4.

Table 4. Parameters for the rod model.

Easting (m)	Northing (m)	Depth (m)	Inc	Dec	Moment	Aspect
3.5	2.5	1.0	0.0	0.0	0.078125	1x5x1
6.5	2.5	1.0	0.0	90.0	0.078125	5x1x1
9.5	2.5	1.0	90.0	*	0.078125	1x1x5
3.5	5.0	1.0	0.0	0.0	0.093750	1x3x1
6.5	5.0	1.0	0.0	90.0	0.093750	3x1x1
9.5	5.0	1.0	90.0	*	0.093750	1x1x3
3.5	7.5	1.0	0.0	0.0	0.078125	1x1x1
6.5	7.5	1.0	0.0	90.0	0.078125	1x1x1
9.5	7.5	1.0	90.0	*	0.078125	1x1x1

* Because the inclination is vertical, the declination can take on any value

A Helbig-Euler inversion on the vector components without any inducing field was able to recover the locations and magnetizations of nine equivalent dipole sources (table 5). The equivalent dipole sources for the vertically oriented rods are shallow, but below the tops of the rods.

Table 5. Results of Helbig-Euler inversion on the rod model without any inducing field.

Easting (m)	Northing (m)	Depth (m)	Inc	Dec	Moment	Aspect
3.5	2.5	1.0761	-2.7667	0.0564	0.068555	1x5x1
6.5	2.5	1.4324	0.0766	90.1459	0.120341	5x1x1
9.5	2.5	0.5847	89.8303	22.9334	0.039192	1x1x5
3.5	5.0	0.9547	-0.1952	0.1755	0.073168	1x3x1
6.5	5.0	1.1522	0.2337	90.0532	0.111400	3x1x1
9.5	5.0	0.8358	89.8144	56.1906	0.072610	1x1x3
3.5	7.5	0.9219	0.9035	0.1408	0.062294	1x1x1
6.5	7.5	0.9812	0.0367	90.1043	0.073405	1x1x1
9.5	7.5	0.9952	89.7147	146.2096	0.076875	1x1x1

To simulate the peak response of the active system, a vertical inducing field was applied to the model under the assumption that all sources had a Koenigsberger ratio of 1.0. Table 6 shows the results of a Helbig-Euler inversion on the vector components with the inducing field in the downward direction, and table 7 shows the results on the vector components with the inducing field in the upward direction. Note that the upward-inducing field exactly cancels the field of the three source bodies with vertical remanent magnetization.

Table 6. Results of Helbig-Euler inversion on the rod model with downward-inducing field.

Easting (m)	Northing (m)	Depth (m)	Inc	Dec	Moment	Aspect
3.5	2.5	0.9016	52.54576	0.152	0.0691042	1x5x1
6.5	2.5	1.3690	53.97548	89.669	0.1503845	5x1x1
9.5	2.5	0.5829	89.47509	-4.957	0.0775733	1x1x5
3.5	5.0	0.9764	46.90822	0.974	0.1117457	1x3x1
6.5	5.0	1.1366	47.18464	89.275	0.1494823	3x1x1
9.5	5.0	0.8284	89.64802	2.382	0.1418990	1x1x3

3.5	7.5	1.0266	45.69145	0.225	0.1120025	1x1x1
6.5	7.5	0.9771	45.00643	91.085	0.1032609	1x1x1
9.5	7.5	0.9793	89.30260	175.421	0.1486813	1x1x1

Table 7. Results of Helbig-Euler inversion on the rod model with upward-inducing field.

Easting (m)	Northing (m)	Depth (m)	Inc	Dec	Moment	Aspect
3.5	2.5	1.2782	-54.5383	-0.1704	0.1427875	1x5x1
6.5	2.5	1.3805	-53.9433	90.5759	0.1689254	5x1x1
9.5	2.5	*	*	*	*	1x1x5
3.5	5.0	0.9629	-47.0065	0.0201	0.1133776	1x3x1
6.5	5.0	1.1371	-46.3786	89.8697	0.1578909	3x1x1
9.5	5.0	*	*	*	*	1x1x3
3.5	7.5	0.8343	-43.7581	0.0357	0.0754909	1x1x1
6.5	7.5	0.9796	-44.9590	89.1212	0.1040951	1x1x1
9.5	7.5	*	*	*	*	1x1x1

* No values because the inducing field exactly cancels the remanent field.

The total magnetization vector for each source changes direction and magnitude as a result of the vertical inducing field. The magnetic susceptibility of each source is given by the magnitude of the change in the vertical component of magnetization divided by the inducing field strength. The Koenigsberger ratio Q of each source is the ratio of the remanent magnetization to the induced magnetization. This is equivalent to the ratio of the dipole moment without an inducing field to the product of the magnetic susceptibility and the inducing field strength, or to the ratio of the dipole moment without an inducing field to the magnitude of the change in the vertical component of magnetization. Table 8 shows the estimated magnetic susceptibility and Koenigsberger ratio for each source.

Table 8. Estimated magnetic susceptibilities and Koenigsberger ratios for the rod model.

Easting	Northing	Downward field		Upward field		Average	
		susc	Q	susc	Q	susc	Q
3.5	2.5	0.058167	1.178594	0.112992	0.606725	0.085579	0.892660
6.5	2.5	0.121465	0.990744	0.136726	0.880158	0.129096	0.935451
9.5	2.5	0.038378	1.021210	0.038378	1.021210	0.038378	1.021210
3.5	5.0	0.081853	0.893898	0.082679	0.884969	0.082266	0.889433
6.5	5.0	0.109198	1.020164	0.114754	0.970772	0.111976	0.995468
9.5	5.0	0.069287	1.047956	0.069287	1.047956	0.069287	1.047956
3.5	7.5	0.079165	0.786883	0.053193	1.171093	0.066179	0.978988
6.5	7.5	0.072978	1.005850	0.073601	0.997336	0.073289	1.001593
9.5	7.5	0.071796	1.070750	0.071796	1.070750	0.071796	1.070750

Note that the estimated susceptibilities are close to the true susceptibilities of 0.78 to 0.94, and the estimated Q-values are all close to the true value of 1.0. There is no apparent way to distinguish between the small cube-like bodies that approximate true dipoles and the rod-like sources.

The plate simulation involved three large rectangular plates of dimensions 5 units by 5 units by 1 unit oriented with the normal to the large surface directed along the east, north, and vertical axes; three smaller rectangular plates 3 units by 3 units by 1 unit also oriented along the east, north, and vertical axes; and three 1-unit cubes. One unit equals 0.25 m. The centers of the sources were 4 units below the sensors. The plates had remanent magnetizations oriented along the normal to their larger surfaces, and the three cubes had remanent magnetizations in the three orthogonal directions. The remanent magnetization intensities were set so that the equivalent dipole moments of the sources were roughly the same. The model is described in table 9.

Table 9. Parameters for the plate model.

Easting (m)	Northing (m)	Depth (m)	Inc	Dec	Moment	Aspect
3.5	2.5	1.0	0.0	90.0	0.390625	1x5x5
6.5	2.5	1.0	0.0	0.0	0.390625	5x1x5

9.5	2.5	1.0	90.0	*	0.390625	5x5x1
3.5	5.0	1.0	0.0	90.0	0.421875	1x3x3
6.5	5.0	1.0	0.0	0.0	0.421875	3x1x3
9.5	5.0	1.0	90.0	*	0.421875	3x3x1
3.5	7.5	1.0	0.0	90.0	0.390625	1x1x1
6.5	7.5	1.0	0.0	0.0	0.390625	1x1x1
9.5	7.5	1.0	90.0	*	0.390625	1x1x1

* Because the inclination is vertical, the declination can take on any value.

A Helbig-Euler inversion on the vector components without any inducing field was able to recover the locations and magnetizations of nine equivalent dipole sources (table 10). The equivalent dipole sources for the vertically oriented plates are relatively shallow, and those for the horizontally oriented plates are relatively deep.

Table 10. Results of Helbig-Euler inversion on the plate model without any inducing field.

Easting (m)	Northing (m)	Depth (m)	Inc	Dec	Moment	Aspect
3.5	2.5	0.7774	0.0676	89.981	0.2970	1x5x5
6.5	2.5	0.7160	-0.5427	0.247	0.2464	5x1x5
9.5	2.5	1.5571	89.8123	-33.665	0.7114	5x5x1
3.5	5.0	0.9792	-0.0449	90.001	0.4386	1x3x3
6.5	5.0	0.7851	0.1167	0.354	0.2597	3x1x3
9.5	5.0	1.1787	89.6944	171.477	0.5159	3x3x1
3.5	7.5	1.0852	-0.0978	89.981	0.4616	1x1x1
6.5	7.5	0.8737	0.9159	0.091	0.2781	1x1x1
9.5	7.50	0.9900	89.4207	170.582	0.3841	1x1x1

To simulate the peak response of the active system, a vertical inducing field was applied to the model under the assumption that all sources had a Koenigsberger ratio of 1.0. Table 11 shows the results of a Helbig-Euler inversion on the vector components with the inducing field in the downward direction, and table 12 shows the results on the vector components with the inducing field in the upward direction. Note that the upward-inducing field exactly cancels the field of the three source bodies with vertical remanent magnetization.

Table 11. Results of Helbig-Euler inversion on the plate model with downward-inducing field.

Easting (m)	Northing (m)	Depth (m)	Inc	Dec	Moment	Aspect
3.5	2.5	0.7397	41.73358	88.813	0.3548	1x5x5
6.5	2.5	0.6718	40.81954	1.440	0.2886	5x1x5
9.5	2.5	1.4978	89.33935	-13.967	1.2983	5x5x1
3.5	5.0	0.9209	43.15523	90.048	0.5359	1x3x3
6.5	5.0	0.7983	43.21744	1.092	0.3884	3x1x3
9.5	5.0	1.1664	89.68020	-153.122	0.9993	3x3x1
3.5	7.5	1.0118	45.04357	90.955	0.5629	1x1x1
6.5	7.5	0.9802	45.61699	0.2420	0.5141	1x1x1
9.5	7.5	0.9814	89.49455	178.788	0.7479	1x1x1

Table 12. Results of Helbig-Euler inversion on the plate model with upward-inducing field.

Easting (m)	Northing (m)	Depth (m)	Inc	Dec	Moment	Aspect
3.5	2.5	0.8002	-39.9867	91.77386	0.4271	1x5x5
6.5	2.5	0.7629	-40.0210	0.46948	0.3815	5x1x5
9.5	2.5	*	*	*	*	5x5x1
3.5	5.0	1.0229	-44.7400	88.68530	0.6514	1x3x3
6.5	5.0	0.8054	-44.0549	1.61406	0.3927	3x1x3
9.5	5.0	*	*	*	*	3x3x1
3.5	7.5	1.1291	-45.6148	88.01538	0.6914	1x1x1
6.5	7.5	0.7994	-42.7912	1.14784	0.3404	1x1x1
9.5	7.5	*	*	*	*	1x1x1

* No values because the inducing field exactly cancels the remanent field.

Table 13 shows the estimated magnetic susceptibility and Koenigsberger ratio for each source.

Table 13. Estimated magnetic susceptibilities and Koenigsberger ratios for the plate model.

Easting	Northing	Downward field		Upward field		Average	
		susc	Q	susc	Q	susc	Q
3.5	2.5	0.235834	1.259416	0.274829	1.080720	0.255332	1.170068
6.5	2.5	0.190986	1.290113	0.242988	1.014017	0.216987	1.152065
9.5	2.5	0.586830	1.212255	0.586830	1.212255	0.586830	1.212255
3.5	5.0	0.366857	1.195554	0.458147	0.957328	0.412502	1.076441
6.5	5.0	0.265441	0.978384	0.273612	0.949164	0.269527	0.963774
9.5	5.0	0.483386	1.067227	0.483386	1.067227	0.483386	1.067227
3.5	7.5	0.399088	1.156531	0.493355	0.935549	0.446222	1.046040
6.5	7.5	0.363011	0.766083	0.235662	0.935549	0.299337	0.850816
9.5	7.5	0.363787	1.055894	0.363787	1.055894	0.363787	1.055894

Again the estimated susceptibilities are close to the true susceptibilities of 0.39 to 0.42 and the estimated Q values are all close to the true value of 1.0. There is no apparent way to distinguish between the small cube-like bodies that approximate true dipoles and the plate-like sources.

Engineering Assessment

A conceptual block diagram for the ATMGS is shown in figure 17. Components unique to the ATMGS are the Primary Drive Coil and the Active Drive Unit, which contains the Oscillator Circuitry and the Drive Current Circuitry. The drive current circuit has links to the magnetometer control circuitry, for feedback control, and to the sample and hold in the data acquisition unit, for monitoring of the primary drive current. The engineering assessment focused on the hardware requirements for the active drive unit and the primary drive coil.

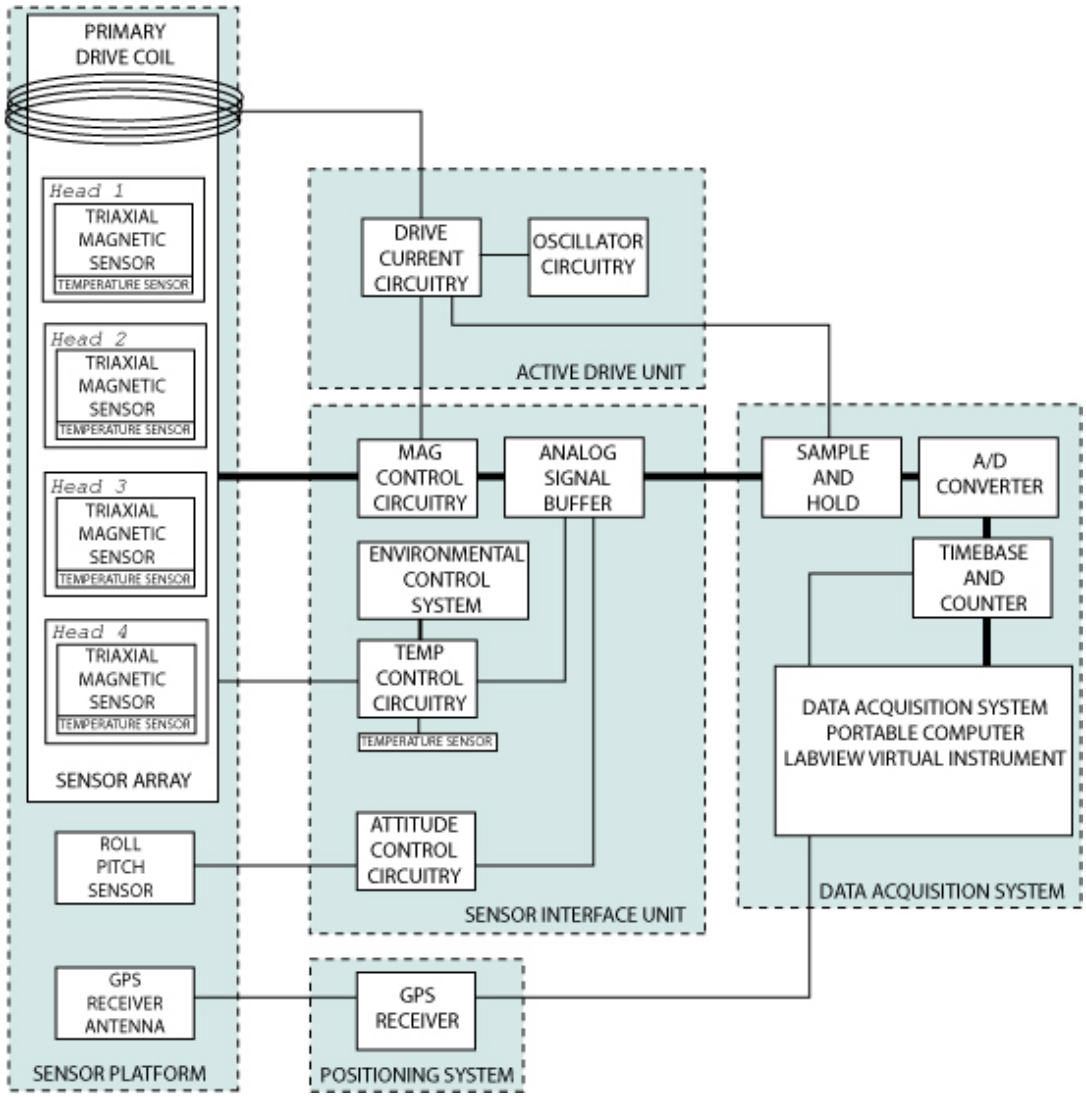

Figure 17. Conceptual block diagram of the ATMGS.

Primary Signal Generator

The object of this task is to design and specify an active constant current drive signal for the ATMGS. The requirements for the system are as follows: the system generates a constant amplitude sine wave magnetic signal of less than 100 Hz, the amplitude being at least 12 amperes peak (8.5 amperes root-mean-squared); the amplitude should remain as constant as possible over a varying temperature range, with minimum distortion; and the coil should fit the existing TMGS cart. In the event this last requirement changes, the calculations can be repeated for different coil geometries. A conceptual block diagram of the active drive unit is given in figure 18.

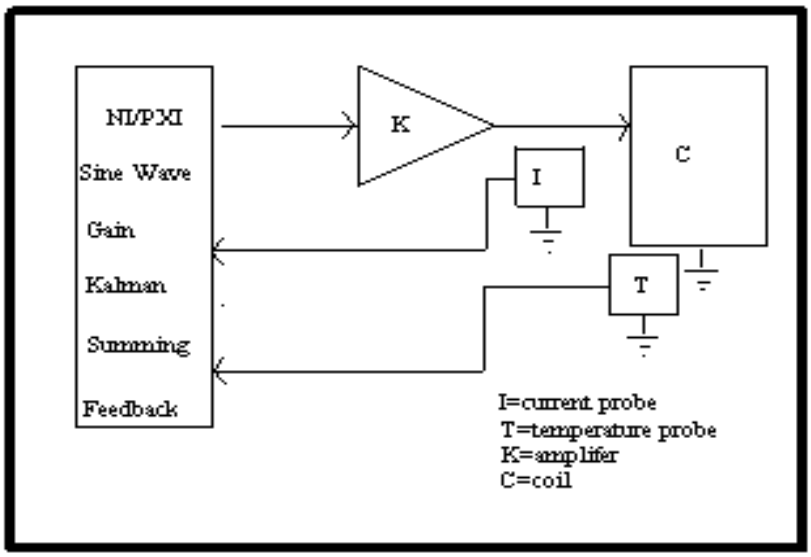

Figure 18. Conceptual block diagram of the active drive unit. Subsystems are labeled NI/PXI, K, I, C, and T. Kalman: See section, "Possible Sources of Improvement (NI/PXI)."

To achieve the design objective, the following specifications were developed for each subsystem:

Coil Parameters (C)
For this analysis a square coil having 45 inches (1.143 m) on a side with a 20-turn tight winding is assumed. If a #10 gauge copper wire is used, the coil will have a resistance of approximately 0.3 Ω at 20°C. The resistance would increase to approximately 0.38 Ω at 60 ^{o}C. The inductance of the coil would be 2.95 mH (Grover web site) giving a reactance of 1.22 Ω at 100 Hz. Therefore, the total worst case impedance would be approximately 1.6 Ω at 60°C and 100 Hz signal input. This coil design would deliver a peak moment magnitude of 15.68 A-m^2.

Amplifier Specifications (K)
A standard class AB audio power amplifier can be used to drive the coil. A typical 4-ohm speaker has a dc (direct current) resistance of 3.3 Ω and an inductance of 2-5 mH. The minimum impedance rating for most audio amplifiers is 4 Ω. Therefore, a noninductive series resistor of approximately 1.7 Ω would be added to increase the overall load to 4 Ω, or 0.4 Ω for a 2 Ω load. With a 4 Ω load, the

amplifier would have to provide 289 watts of continuous power. Using the conventional two-times engineering margin, a 580-watt amplifier at a 4 Ω load is recommended. If a 2 Ω load amplifier is available, the wattage would be reduced to 290 watts. A possible candidate is the Crown Micro-Tech 2400 Professional Power Amplifier, which can supply 1,050 W into a 2 Ω load.

Current Sensor (I)

A standard audio amplifier is a constant voltage device. To make it a constant current system, a voltage representing the output current is used as feedback. Of the current monitoring devices available, a magneto resistive device provides the best linearity, zero crossing linearity, isolation and temperature compensation. An example of such a device is the NT-15 from F.W. Bell. It states a linearity of less than 0.1 percent and a bandwidth of 100 kHz.

Sine Wave Source

The existing National Instruments (NI) PXI system (National Instruments web site) can be used as a signal source for the sine wave. The NI system can also be used as the feedback point. This provides a flexible feedback system for possible improvement exploration, should that be necessary. The inaccuracy of the raw sine wave in LabView (NI's software development system) was measured at 5E-10 for a 1-volt output or 0.5 ppb. Using a 24-bit D/A to output the signal produces an uncertainty of 6E-8 or 60 ppb. A 16-bit D/A would be 1.5E-5 or 15 ppm.

Temperature Control (T)

Another factor requiring compensation would be the thermal expansion of the coil. With a possible increase of 0.13 percent in area over a 40°C temperature range, a feedback control to adjust the current to compensate for this is needed. A temperature probe providing feedback should accomplish this. The resolution of an existing probe is 0.1^{o}C. Over 40°C, this would give a resolution of one part per 1,000. This implies a resolution of 1.3E-6 or 1.3 ppm temperature compensation.

Possible Sources for Improvement (NI/PXI)

The use of the NI /PXI package to develop the appropriate feedback gains and summing allows for the possible use of a Kalman filter to increase the accuracy of the current. A Kalman filter (Simon, 2003; Bishop, 2001; Cipra, 1993) provides increased accuracy in the presence of white (Gaussian) noise if the system is linear. Such is the case for this system.

For an active magnetic system, canceling the portion of the magnetic field from the primary drive coil would be necessary. For an ATMGS with the drive coil surrounding the magnetometer array, the field strengths and gradients at the sensors would be considerable, as illustrated in figure 19.

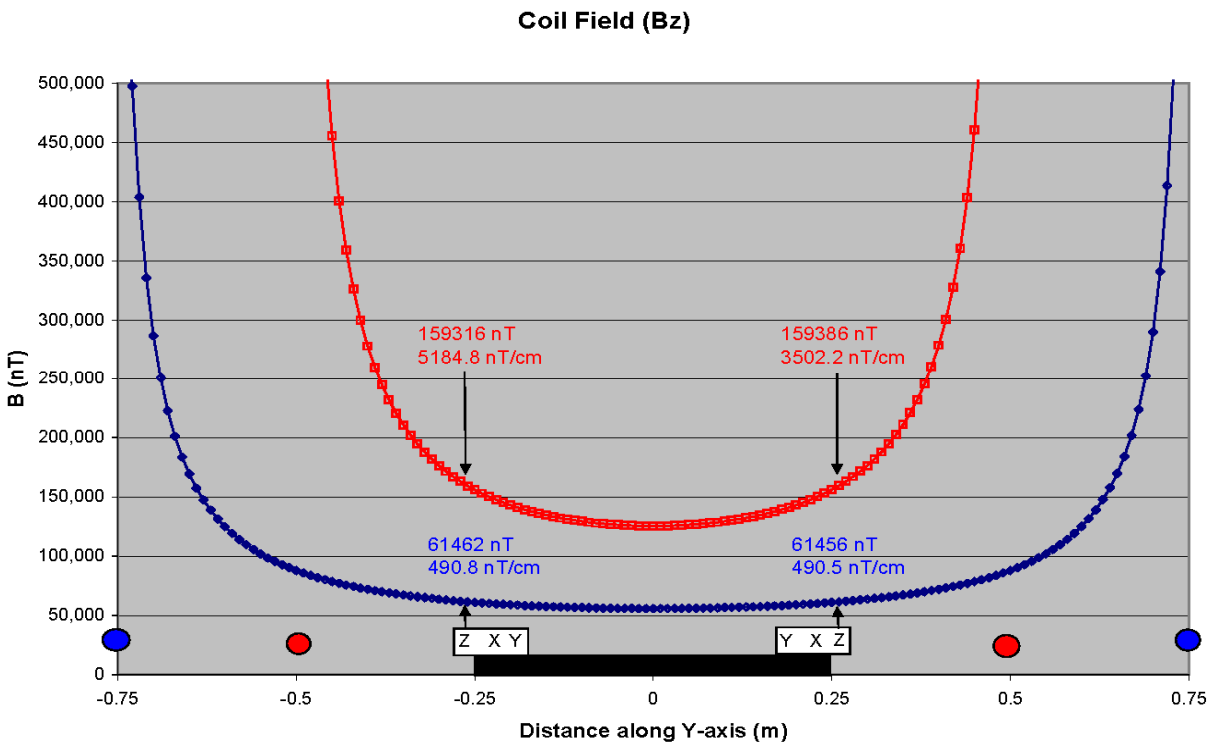

Figure 19. The black rectangle represents the array baseplate; the white rectangles represent fluxgate heads. Magnetic field strength is plotted for a 1.0-m diameter coil (red) and a 1.5-m diameter coil (blue). Arrows point to the field strength and gradient at the location of the z-component fluxgate axes.

Three nulling methods are considered: numerical subtraction, a bucking coil, and use of the existing feedback coils contained in each ring core sensor.

Numerical Subtraction

From the design of the controlled sine wave generator, we would have an accurate measure of the drive current, hence an estimate of the field strength at the magnetometers. Using the field strength value and scaling it, we can get a value for the field at the magnetometer's heads. As long as this field is in the range of the existing fields (mainly the Earth's magnetic field), we can subtract it from the received signal. This method would be straightforward to implement in software or post-processing, and success could be accurately determined through laboratory experiments. However, this method would be unable to compensate for unexpected changes in field strength or direction, such as would be caused by misalignment of the primary coil and the sensor array. Mechanical deformations and misalignments are difficult to control during operation over real terrains. Just as the sensor array must be calibrated in a controlled magnetic environment, the primary coil/array interaction would need to be calibrated in a

controlled setting. Because it is not known how the ring-core fluxgate sensors would perform in a harsh magnetic environment (high fields, high gradients, high slew rate), this method is not recommended.

Bucking Coil

A bucking coil would be a separate coil encompassing the entire magnetometer array and driven by a scaled, reversed value of the drive current so as to provide a magnetic well where the drive fields are neutralized. Several versions of this are possible. One would use the drive current with the coil wound in reverse and the number of turns adjusted to compensate for the difference in the area of the two coils. In principle this method is the best, because it would be simple to implement electronically. Only one drive amplifier would be required, and there would be no additional software controls. On the other hand, this method would be difficult to implement mechanically (the sensor array, the primary field coil, and the bucking coil would have to be maintained in rigid alignment), it would be difficult to tune or adjust, and it would be difficult to wind an accurate, large bucking coil and position it so that all 12 magnetic axes are nearly nulled. Furthermore, the primary coil/bucking coil/array interaction would need to be calibrated in a controlled setting.

An alternative design would be to drive the bucking coil with another amplifier whose input signal is derived from the active drive unit. This would offer easy current adjustment, with the possibility of adjusting the current dynamically. However, two amplifiers are required, with more complexity in the electronics and software development. Mainly because of difficulties with fabrication and mechanical stability, neither of these methods is recommended.

Ring-Core Feedback

A variation on the bucking coil would be to use existing ring core feedback circuits and insert bucking currents directly to each magnetic field sensor (Magnes and others, 2003). This scheme can provide current compensation to all 12 magnetic components without the need for a large external bucking coil. Individual bucking currents would be determined from empirical measurements (nulling tests) in a controlled magnetic environment. Offsetting the advantage this method offers is increased electronic complexity and the possibility that tapping into the feedback circuit of the existing interface electronics would create unforeseen problems. Because of its fundamental simplicity, this method is recommended as the first approach.

Alternative Sensor Technologies

In evaluating alternative fluxgate magnetometers, a literature review led to the following technical papers deemed most relevant to our engineering evaluation:

- Advanced Composition Explorer (ACE) Magnetometer Instrument (MAG) (Bartol Research Institute, 1994)
- Development, construction and analysis of the `Orsted' fluxgate magnetometer (Nielsen and others, 1995)
- Digital detection and feedback fluxgate magnetometer (Piil-Henriksen and others,1996)
- New kind of fluxgate magnetometer probe with enhanced electronic processing (Cruz and others, 1998)
- Fluxgate: Tuned vs. untuned output (Ripka, 1998)
- Portable fluxgate magnetometer (Ripka and Kaspar, 1998)

- Digital Fluxgate for the Astrid-2 satellite (Pedersen and Primdahl, 1999)
- Ring-core flux-gate magnetometer with microprocessor (Kilić and others, 1999)
- Magnetic field measurements in space: The NewMag Magnetometer (Bish and others, 2000)
- Crossfield effect at fluxgate (Ripka and Billingsley, 2000)
- Comparison of two digital fluxgate magnetometers developed for space application (Magnes and Auster, 2001)
- A digital fluxgate magnetic sensor interface using sigma-delta modulation for weak magnetic field measurements (Kawahito and others, 2002)
- The fluxgate ring-core internal field (Primdahl and others, 2002), and
- A sigma-delta fluxgate magnetometer for space applications (Magnes and others, 2003).

A miniaturized ATMGS is proposed based upon existing equipment and state-of-the-art practices described in the listed articles. The system would consist of the existing Narod triaxial fluxgate heads and cables, a 24-bit analog-to-digital converter (A/D), a digital signal processor (DSP), a 24-bit digital-to-analog converter (D/A) for the primary drive waveform and bucking-coil current feedback, and a wireless communication system to receive commands and send data to a remote computer. Commercial 24-bit A/D and D/A units are widely available and cost effective. They can provide flexibility in determining the maximum quantization necessary from the input and feedback signal. They are capable of 200 kHz sample rates, should that be necessary. If time and resources permit, the fluxgate interface electronics would be enhanced using one of the methods mentioned in the articles. A DSP can be programmed from a LabView software program. This provides quick turn-around during development. It also provides an ability to try various methods of signal extraction. For example, all even harmonics or just the 2nd harmonic, use of a FIR filter to cancel all odd harmonics or an analog bandpass filter or both, using a fast Fourier transform to analyze the received signal, use of a binning technique for feedback control, direct read-out without feedback, and adjustable bandwidth. The unit could be set up to transmit the data wirelessly to a remote station using one of the current technologies such as Bluetooth, Wi-Fi, or ZigBee. ZigBee might not handle the data volume required, but it would provide built-in data collision prevention from many sources.

Other sensor types evaluated included the following:

- Proton and Overhauser magnetometers are scalar instruments, heavy, high power; satellite Overhauser weights 1 kg and requires 3 W of power
- High temperature SQUIDS have lower noise but require liquid nitrogen
- Hall sensors are noisy and have temperature-dependent offsets
- Magnetodiodes and magnetoresistors perform no better than Hall sensors of the same size
- GMI (Giant Magnetoresistors and Giant Magnetoinductance) effects are weak and impractical
- GMR (Giant Magnetoresistor) has parabolic characteristics and 4 percent hysteresis and nonlinearity, expensive electronic compensation is required
- AMR (Anisotropic Magnetoresistors) work well in the flipping mode, but have high noise.

Based upon the foregoing evaluation of current magnetic sensor technology, keeping the Narod Geophysics triaxial ring-core fluxgates in the ATMGS design is therefore recommended.

Conclusions

In this research we have demonstrated the advantages of an active tensor magnetic gradiometer system (ATMGS) which operates as a dual-mode survey system. In the first (static) mode, the ATMGS performs as a magnetic gradient system that provides both vector and total field magnetic measurements. These data can be processed using conventional software based upon potential fields theory. In the second (active) mode, the ATMGS measures the secondary magnetic fields produced by a primary field generator. These secondary fields are caused by induced magnetic moments, which themselves are function of a target's composition, location, and shape. Spheroidal ferrous targets closely approximate intact UXO (unexploded ordnance). Therefore, if a target produces secondary fields distinctive of a spheroidal body, it can be classified as UXO-like, as opposed to rod-like or plate-like bodies. We have shown that the ATMGS data can be inverted to obtain spheroidal dimensions, and that it is possible on this basis to distinguish between the different types of body geometry. However, we have also shown that it is not possible to separate the induced and remanent moments of a magnetically permeable body using ATMGS data.

Implementation of the ATMGS in hardware is feasible, but placing fluxgate magnetometers inside a powerful primary field coil poses difficult engineering problems. Foremost is the need to partially or fully cancel the primary field at the location of the fluxgate cores. The most sensible approach is to add a cancellation current directly to the fluxgate drive coil. Whether this can be done successfully with existing feedback and interface electronics is unknown. Designing and fabricating a solenoid centered on a large sensor array that can maintain structural rigidity during field deployment would require a major effort. Furthermore, the primary coil/sensor array combination would have to be accurately calibrated to compensate for inorthogonalities and asymmetries. Calibrating the TMGS has proven to be both troublesome and time-consuming. Calibration data must be acquired at a controlled magnetic site using specialized experimental assemblies, and data processing to derive accurate calibration coefficients has not been streamlined.

References Cited

Altshuler, T.W., 1996, Shape and orientation effects on magnetic signature prediction for unexploded ordnance: Proceedings of the UXO forum ’96, Williamsburg, Va., p. 282-291.

Bartol Research Institute, 1994, Advanced Composition Explorer (ACE) Magnetometer Instrument (MAG) Instrument Functional Requirement Document (IFRD): Newark, Del., University of Delaware

Billings, S.D., 2002, UXO discrimination and identification using magnetometry: Proceedings of the Society for the Application of Geophysics to Engineering and Environmental Problems (SAGEEP), Las Vegas, Nev.

Bish A., Fraser, B.J., Menk, F.W., Waters, C.L., Means, J.D., and Russell, C.T., 2000, Magnetic field measurements in space – The NewMag Magnetometer: Proceedings of the Workshop on Applications of Radio Science (WARS’00), p. 160-169.

Bishop, G., 2001, An introduction to the Kalman filter: SIGGRAPH 2001 Course 8, Association for Computing Machinery, Inc., SIGGRAPH 2001, Los Angeles, Calif.

Butler, D.K., 2001, Potential fields methods for location of unexploded ordnance (UXO): The Leading Edge, August 2001, 6 p.

Cipra, B., 1993, Engineers look to Kalman filtering for guidance: Society for Industrial and Applied Mathematics (SIAM) News, v. 26, no. 5.

Cruz, J.C., Trujillo, H., and Rivero, M., 1998, New kind of fluxgate magnetometer probe with enhanced electronic processing: Sensors and Actuators, A: Physical, v. 71, no.3, p. 167-171.

Grover, F.W., "Inductance Calculations", *http:// emclab.mst.edu/inductance/index.html* [accessed on Dec. 21, 2007]

Helbig, K., 1963, Some integrals of magnetic anomalies and their relation to the parameters of the disturbing body: Zeitschrift für Geophysik, v. 29, no.2, p. 83-96.

Kawahito, S., Cerman, A., and Tadokoro, Y., 2002, A digital fluxgate magnetic sensor interface using sigma-delta modulation for weak magnetic field measurements: Instrumentation and Measurement Technology Conference, Proceedings of the 19th IEEE, p. 257-260.

Kilić, T., Boršić, M., and Milun, S., 1999, Ring-core flux-gate magnetometer with microprocessor: Measurement – Journal of the International Measurement Confederation, v. 25, no. 1, p. 47-51.

Magnes, W., and Auster, H., 2001, Comparison of two digital fluxgate magnetometers developed for space application: Contributions to Geophysics and Geodesy, v. 31, p. 67-74.

Magnes, W., Pierce, D., Valavanoglou, A., Means, J., Baumjohann, W., Russell, C.T., Schwingenschuh, K., and Graber, G., 2003, A sigma-delta fluxgate magnetometer for space applications: Measurement Science and Technology, v. 14, p. 1003-1012.

National Instruments, *http://www.ni.com/pdf/products/us/pxi4461.pdf* [accessed on Dec. 21, 2007]

Nielsen, O.V., Petersen, J.R., Primdahl, F., Brauer, P., Hernando, B., Fernandez, A., Merayo, J.M.G., and Ripka, P., 1995, Development, construction and analysis of the `Orsted' fluxgate magnetometer: Measurement Science and Technology, v. 6, no.8, p. 1099-1115.

Pedersen, E.B., and Primdahl, F., 1999, Digital fluxgate magnetometer for the Astrid-2 satellite: Measurement Science and Technology, v. 10, p. N124-N129.

Phillips, J.D., 2005, Can we estimate total magnetization directions from aeromagnetic data using Helbig's integrals?: Earth, Planets and Space, v. 57, no.8, p. 681-689.

Phillips, J.D., Nabighian, M.N., Smith, D.V., and Li, Y., 2007, Estimating locations and total magnetization vectors of compact magnetic sources from scalar, vector, or tensor magnetic

measurements through combined Helbig and Euler analysis: Society of Exploration Geophysics Expanded Abstracts v. 26, p. 770.

Piil-Henriksen, J., Merayo, J.M.G., Nielsen, O.V., Petersen, H., Raagaard Petersen, J., and Primdahl, F., 1996, Digital detection and feedback fluxgate magnetometer: Measurement Science and Technology, v. 7, p. 897-903.

Primdahl, F., Brauer, P., Merayo, J.M.G., and Nielsen, O.V., 2002, The fluxgate ring-core internal field. Measurement Science and Technology, v. 13, no.8, p. 1248-1258.

Reid, A.B., Allsop, J.M., Granser, H., Millett, A.J., and Somerton, I.W., 1990, Magnetic interpretation in three dimensions using Euler deconvolution: Geophysics, v. 55, p. 80-91.

Ripka, P., 1998, Fluxgate – Tuned vs. untuned output: IEEE Transactions on Magnetics, v. 34, no. 4 part 1, p. 1303-1305.

Ripka, P., and Kaspar, P., 1998, Portable fluxgate magnetometer: Sensors and Actuators A–Physical, v. 68, nos. 1-3, p. 286-289.

Ripka, P., and Billingsley, S.W., 2000, Crossfield effect at fluxgate: Sensors and Actuators A–Physical, v. 81, no. 1, p. 176-179.

Schmidt, P.W., and Clark, D.A. 1997, Directions of magnetization and vector anomalies derived from total field surveys: Australian Society of Exploration Geophysicists Preview, v. 70, p. 30-32.

Schmidt, P.W. and Clark, D.A., 1998, The calculation of magnetic components and moments from TMI – A case history from the Tuckers igneous complex: Queensland, Exploration Geophysics, v. 29, p. 609-614.

Simon, D., 2003, Kalman filtering for fuzzy discrete time dynamic systems: Applied Soft Computing, v. 3 (2003), p. 191–207.

Zhang, C., Mushayandebvu, M.F., Reid, A.B., Fairhead, J.D., and Odegard, M.E., 2000, Euler deconvolution of gravity tensor gradient data: Geophysics, v. 65, p. 512-520.